TÉCNICO LISBOA

Synthesis and precipitation of silica and titania nano-structures on cellulose fibers by biomineralization processes

Verónica de Carvalho Roque Bouça

Thesis to obtain the Master of Science Degree in

Bioengineering and Nanosystems

Supervisor: Prof. Duarte Miguel de França Teixeira dos Prazeres

Examination Committee

Chairperson: Prof. Gabriel António Amaro Monteiro

Supervisor: Prof. Duarte Miguel de França Teixeira dos Prazeres

Members of the committee: Prof. Luís Joaquim Pina da Fonseca

May 2016

Acknowledgements

First of all, as I am finishing an important step in my life, I would like to thank all the people who supported me during this final project.

A special thank you to Prof. Dr. Miguel Prazeres for giving me this opportunity, for all the patience and for the crucial motivation during this work.

To all my colleagues from the lab, specially to Ana Rosa and Claudia Alves for the advices and for helping me in different stages of my work. Without them this work would not have been so easy.

I want to leave a huge thank you to my parents who always believed in me, encouraged me to take on new challenges, and without whom I would have never come here.

Finally, I want to thank my friends, specially Ricardo Carvalho, José Cardoso, Ana Catarina, Emanuel Capela, Flavio Ferreira, Alexandra Wagner, and Ayewa Agognon for all the support and for being there by my side on the best and worst moments of this trial.

Thank you all.

Resumo

O objetivo desta dissertação foi desenvolver materiais híbridos de celulose/sílica e celulose/dióxido de titânio para explorar o processo de biomineralização do péptido R5 (SSKKSGSYSGSKGSKRRIL). A primeira etapa consistiu no estudo da precipitação de nanopartículas de sílica e dióxido de titânio pelo R5 em solução. Nas condições estudadas (1,5 mM R5, 91 mM precursor, pH 7), a atividade especifica do R5 para precipitação de sílica e dióxido de titânio foi 8,6 ± 2,2 nmol Si/min.nmol e 6,0 ± 1,0 nmol Ti/min.nmol R5, respetivamente. Analise no SEM mostrou que os precipitados eram compostos por nanopartículas sensivelmente esféricas com tamanhos individuais na ordem dos 37 e 538 nm para a sílica, sendo para o dióxido de titânio na ordem de 479 nm. As experiencias que resultaram da fusão do R5 com módulo de ligação a carbohidratos (CBM3) confirmaram que o R5 mantem a sua capacidade de precipitar sílica e dióxido de titânio, produzindo nanopartículas com tamanhos e morfologias comparáveis. Foi investigada a capacidade do R5 e CBM3-R5 para precipitar sílica e dióxido de titânio *in situ* sobre fibras de celulose. Quando foi utilizada uma quantidade de 3000 pmol/0,13 cm^2, tanto o R5 (via adsorção física) e o CBM3-R5 (por interações e afinidade), ambos pré-imobilizados, foram capazes de precipitar sílica produzindo densas estruturas contendo partículas de sílica fundidas e aglomeradas sob as fibras de celulose. As partículas individualizadas que foram obtidas com o R5 e CBM3-R5 apresentaram um tamanho medio na ordem de 213 ± 78 nm e 231 ± 39 nm, respetivamente.

Palavras-chave: Nanopartículas, sílica, dióxido de titânio, proteína CBM3-R5, papel

Abstract

The goal of this thesis was to develop hybrid materials of cellulose/silica and cellulose/titanium dioxide by exploring the biomineralization ability of the peptide R5 (SSKKSGSYSGSKGSKRRIL). As a first step, the R5-induced precipitation of silica and titanium dioxide nanoparticles in solution was studied. Under the conditions studied (1.5 mM R5, 91 mM precursor, pH 7), the specific activity of R5 for silica and titanium dioxide precipitation was 8.6 ± 2.2 nmol Si/min.nmol R5 and e 6.0 ± 1.0 nmol Ti/min.nmol R5, respectively. SEM analysis showed that precipitates were composed of close to spherical nanoparticles with two individual sizes in the order of 37 and 538 nm for silica; for the titania case, they were in the order of 479 nm. Experiments conducted with a fusion of R5 with a carbohydrate binding module (CBM3) confirmed that R5 maintained its ability to precipitate silica and titanium dioxide, yielding nanoparticles with comparable morphology/size. The ability of R5 and CBM3-R5 to precipitate silica and titanium dioxide *in situ* paper fibers investigated. When used an amount of 3000 pmol/0.13 cm^2, both pre-immobilized R5 (via physical adsorption) and CBM3-R5 (by affinity interactions) were able to precipitate silica, yielding densely packed networks of fused and clustered particles over the cellulose fibers and fibrils in paper. Individual particles obtained with R5 and CBM3-R5 had an average size of around 213 ± 78 nm and 231 ± 39 nm, respectively.

Keywords: Nanoparticles, silica, titanium dioxide, CBM3-R5 protein, paper

List of contents

1. **Introduction** ... 1

1.1. Nanoparticles ... 1

1.2. Chemical and physical properties ... 2

1.2.1. Chemical and physical properties of SiNPs and their applications ... 2

1.2.2. Chemical and physical properties of TiNPs and their applications ... 3

1.3. Methods for SiNPs and TiNPs synthesis ... 4

1.3.1. Abiotic route for SiNPs/TiNPs synthesis ... 4

1.3.1.1. Sol-gel method ... 4

1.3.1.2. Chemical vapor deposition ... 5

1.3.2. Biomimetic approach based on diatom frustules ... 6

1.3.2.1. Diatom algae ... 6

1.3.2.2. Biosilicification in diatom cell cycle ... 7

1.3.2.3. Organic constituents of diatom biosilica ... 8

1.3.2.4. Silaffins proteins ... 9

1.3.2.5. Model for silica precipitation by silaffins ... 11

1.3.2.6. Biomimetic templates based on biosilicification diatom algae ... 13

1.3.2.7. The role of synthetic R5 peptide ... 14

1.4. Applications of R5 ... 17

1.5. Hybrid organic-inorganic composites ... 18

1.5.1. Silica/cellulose and titanium dioxide/cellulose hybrid composite ... 19

1.6. Carbohydrate-binding modules ... 20

1.6.1. Cellulose-binding module family 3 ... 21

1.6.2. Applications of recombinant CBM ... 23

2. **The goal of this work** ... 25

3. **Materials and methods** ... 27

3.1. Materials ... 27

3.1.1. Reagents ... 27

3.1.2. Recombinant Protein CBM3-R5 ... 27

3.2. Methods ... 27

3.2.1. Synthesis of recombinant protein CBM3-R5 ... 27

3.2.2. Purification of recombinant protein CBM3-R5 ... 29

3.2.3. CBM3-R5 protein concentration and exchange buffer ... 30

3.2.4. Silica precipitation assay ... 30

3.2.5. Titanium oxide precipitation assay 30
3.2.6. Determination precipitate yield 30
3.2.7. Silica quantification by β-silicomolybdate spectrophotometric method 31
3.2.7.1. The blue silicomolybdic assay 31
3.2.8. Titanium supernatant quantification by spectrophotometric assay with tiron 32
3.2.9. Scanning Electron Microscopy 33
3.2.10. Dynamic light scattering 33
3.2.11. Silica/Titanium dioxide precipitation on paper via CBM-R5 and R5 34
3.2.11.1. Chromatograhpy paper 34
3.2.11.2. Silica and titanium dioxide precipitation on the paper 34
3.2.11.3. The evaluation of the R5 immobilization via CBM3 or via physical adsorption 35
4. **Results and discussion** 37
4.1. Precipitation of silica induced by the R5 peptide 37
4.2. Size measurements of SiNPs conducted by DLS 38
4.3. Size and morphology of SiNPs analyze through SEM 41
4.4. Precipitation of titanium dioxide induced by R5 42
4.5. Size measurements of TiNPs conducted by DLS 43
4.6. Size and morphology of TiNPs analyze by SEM 46
4.7. Precipitation of silica and titanium dioxide by CBM3-R5 46
4.8. Precipitation of SiNPs on paper via CBM-R5 and R5 48
4.8.1. Immobilization of R5 on the paper 48
4.8.2. Silica precipitation on the paper 50
5. Conclusions 55
References 57

List of Figures

Figure 1. Electron microscopy images of cell wall structures from different diatom species. Species: Stephanopyxis turris, Eucampia zodiacus,Thalassiosira pseudonana(Kröger and Brunner, 2014). 6

Figure 2. Biosynthesis in silica cell wall of diatoms (schematic). The cells are shown in cross-section. This scheme shows the different stages of the cell cycle. 1. The diatom cell has the maximum number of girdle bands; 2. Following cytokinesis, each sibling protoplast (grey) produces new biosilica (red) inside a valve SDV that gradually grows due to accumulation of silica; 3. Complete valve formation into SDV; 4. The complete valves are deposited on the diatom cell surface via exocytosis; 5. Separation of the sibling cells; 6. In order to expand the volume of the protoplast, new silica (blue) is formed within girdle band SDV; 7. During cell growth, several girdle bands are released to the lateral surface by exocytosis; a new cell division starts when the cell volume reaches its maximum. Figure taken from (Sumper and Kröger, 2004; Lechner and Becker, 2015). 8

Figure 3. The amino acids sequence of polypeptide sil1p. Italic letters (residues 1 to 19 residues) represent the typical signal sequence followed by a peptide sequence (residues 20 to 107) that contain a large amount of acidic residues. The COOH-terminal domain is represented by bold letters with boxed lysine residues and arginine. R1 to R7 are the seven homologous repeating unit amino acids (Kröger et al., 1999). A, Ala; C, Cys; D, Asp; E, Glu; F, Phe; G, Gly; I, Ile; K, Lys; L, Leu; M, Met; N, Asn; Q, Gln; R, Arg; S, Ser; T, Thr; V, Val; and Y, Tyr. Figure taken from (Kröger et al., 1999). 9

Figure 4. Chemical structure of NaSil-1A1. The charge represented is an attempt for the solution with pH=5. Post-translational modifications of lysine residues: oligo-N-methy-propylamine (K15 and K3), ε-N,N-dimethyllysine (K4), phosphorylated ε-N,N,N-trimethyl-δ-hydroxylysine (K12). All of the serine residues are phosphorylated.). A, Ala; C, Cys; D, Asp; E, Glu; F, Phe; G, Gly; I, Ile; K, Lys; L, Leu; M, Met; N, Asn; Q, Gln; R, Arg; S, Ser; T, Thr; V, Val; and Y, Tyr. Figure taken from (Sumper and Kröger, 2004). 10

Figure 5. Chemistry of silica. Formation of a sol when pH is above 7, formation a gel when pH is below 7 and precipitation of the colloidal silica particles when a flocculant is added. Figure taken from (Lechner and Becker, 2015). 12

Figure 6. Proposed mechanism for silaffin peptide-mediated poly-condensation reaction of silicic acid through its polyamine groups (Lechner and Becker, 2015). 13

Figure 7. The structural formula of lysine amino acid at pH 7. Figure taken from (Nelson and Cox, 2004). 15

Figure 8. The proposed model for silica precipitation mediated by R5 peptide. Figure taken from (Lechner and Becker, 2014). 15

Figure 9. Silica precipitation as a function of R5 concentration and pH. All experiments used 50 mM silicic acid. Figure taken from (Senior et al., 2015). 16

Figure 10. Schematic representation of the C. thermocellum cellulosome. The cbm3a is connected to the substrate cellulose and to two cohesins (Coh). There are nine highly homologous Coh modules binding to dockerin (Doc) modules, which can interact with the 70 possible glycoside hydrolases (GHs) into the cellulosome. The cellulosome is attached to the cell wall via a surface layer homology (SLH)-like module of an anchoring scaffolding. Figure taken from (Yaniv et al., 2013). 22

Figure 11. Ribbon diagram of the CBM3 from C. thermocellum CipA. Figure taken from (Tormo et al., 1996). 22

Figure 12. Three-dimensional structure of CBM3a The aromatic residues are colored purple. Figure taken from (Blake et al., 2006). 23

Figure 13. Recombinant CBM fusion technology A) fusion of genes coding for CBM and for the desired protein. The C-terminal or N-terminal of the target gene can be used to clone CBM, the fusion on N-terminal is represented here. B) Insertion of the gene into a plasmid vector. (C) Overexpression of the recombinant protein. (D) Purification of the recombinant protein by metal affinity chromatography using the attached his-tag (a tail of six histidines). (E) The protein is released from CBM link to support by proteolytic cleavage of the engineered sequence located between them. This aims to the application of CBM-free protein or peptide. (F) The recombinant protein is eluted from support, to be used for future applications. (G) The immobilized recombinant protein is directly promoting the link for a ligand or a substrate. Figure taken from (Oliveira et al., 2015) 23

Figure 14. Amino acid sequence of CBM3-R5 with199 residues. CBM3, R5 and his tag..... 27

Figure 15. Determination of silicic acid by the silicomolybdic acid spectrophotometric method (blue assay). 32

Figure 16. Determination of titanium by the Tiron complexation assay spectrophotometric method. 33

Figure 17. Silica precipitation with 1.5 mM R5 and 91 mM silicic acid at pH 7 (left). A control was performed without the addition of R5 7 (right). 37

Figure 18. Size distribution of silica particles obtained by precipitation with R5. Determinations were made by analyzing ~ 0.2 mg of silica suspended in 1 ml of water by DLS. The histograms of the number-size distribution (a, b, c) correspond to three measurements made on the same sample. 39

Figure 19. SEM micrographs of SiNPs induced by R5. The A, B and D have a scale bar of 1 µm and C has a scale bar of 100 nm. B and D have micrographs at magnification of x 10,000. A and C have magnifications of x 5,000 and x 30,000, respectively. Arrows indicate three different main populations of morphologies/size of SiNPs. The circles indicate what seems to be fused small particles into a large particle (blue circle) and fusion between two particles (orange circle). 41

Figure 20. Titanium dioxide precipitation with 1.5 mM R5 and 91 mM titanium precursor at pH 7 (right). A control was performed without the addition of R5 7 (right). 42

Figure 21. Size distribution of titanium dioxide particles obtained by precipitation with R5. Determinations were made by analyzing ~ 0.12 mg of titanium dioxide suspended in 1 ml of water by DLS. The histograms of the number-size distribution (a, b, c) correspond to three measurements made on the same sample. 44

Figure 22. SEM micrographs of TiNPs induced by R5. Scale bar of 1 µm. A and B micrographs have magnifications of x 10, 000 and x 5, 000, respectively. 46

Figure 23. SEM micrographs of SiNPs induced by CBM3-R5 in 50 mM phosphate buffer at pH 7. Micrographs were obtained with magnifications of x 1, 500 (A), x 5, 000 (B) and x 10, 000 (C, D). Scale bar corresponds to 10 µm in A and to 1 µm in B-D. 47

Figure 24. SEM micrograph of TiNPs induced by CBM3-R5 in 50 mM phosphate buffer at pH 7 (scale bar of 1 µm). Micrographs were obtained with magnifications of x 5, 000 (A, C) and x 10, 000 (B). 48

Figure 25 Fluorescence intensity obtained by R5 physically adsorption and R5 immobilized by CBM3. Red color corresponds to fluorescence intensity before the immersion on the phosphate buffer 50 mM, pH 7 and the grey color correspond to the fluorescence intensity after the immersion. Photos were taken under UV light (253 nm) 1-CBM3-R5 before the immersion, 2-CBM3-R5 after the immersion, 3-R5 before the immersion, 4- R5 after the immersion and 5- control with 50 mM phosphate buffer pH 7. 49

Figure 26. Composite image of SEM micrographs of circular areas of paper prepared with 3000 nmol of R5 (left) and CBM3-R5 (right), and after immersion on a 91 mM silicic acid solution for 5 min. The formation of silica over paper is apparent by the presence of a whitish material that contrasts strongly with the paper background. Scale bar of 1 mm. 51

Figure 27. SEM micrographs of circular areas of paper prepared with 3000 pmol of R5 (left) and CBM3-R5 (right), and after immersion on a 91 mM silicic acid solution for 5 min. Micrographs were obtained with magnifications of x 5, 000 (A, B) and x 15, 000 (C, D). Scale bar of 1 µm. 51

Figure 28. SEM micrographs of circular areas of paper prepared with 3 pmol of R5 after immersion on a 91 mM silicic acid solution for 5 min. A, B, C micrographs are presented with magnifications of x 5, 000, x 10, 000 and x 1, 000, respectively. Scale bar of 1 µm. 52

List of Tables

Table 1. Experimental conditions used in the R5-induced precipitation of silica and titanium dioxide in 50 mM phosphate, pH 7. Eight independent precipitations experiments were performed for silica and titanium dioxide.. 37

Table 2. R5-induced precipitation of silica in 50 mM phosphate buffer, pH7. A precipitation time of 5 minutes was used. The results shown correspond to averages of eight independent precipitation experiments. 38

Table 3. Average size of silica particles prepared by precipitation with R5 as obtained by DLS. Three size measurements (a, b, c) were performed for a silica sample re-suspended (~0.2 mg) in 1 mL of milli-Q water and subjected to: #1 –no treatment, 2# - ultrasonic treatment for 3 minutes and 3# - 1:4 dilution and ultrasonic treatment for 3 minutes. The mode is shown for each measurement. In some cases, two populations were detected the corresponding number percentage for each sub-population is shown in brackets. The average of the mode obtained is also shown alongside with the mean PDI value. 40

Table 4. R5-induced precipitation of titanium dioxide in 50 mM phosphate buffer, pH 7. A precipitation time of 5 min was used. The results shown here correspond to averages of eight 43

Table 5. Average size of titanium dioxide particles prepared by precipitation with R5 as obtained by DLS. Three size measurements (a, b, c) were performed for a titanium dioxide sample re-suspended (~0.12 mg) in 1 mL of milli-Q water and subjected to: #1 – no treatment, 2# - ultrasonic treatment for 3 minutes and 3# - 1:4 dilution and ultrasonic treatment for 3 minutes. The mode is shown for each measurement. In some cases, two populations were detected - the corresponding number percentage for each sub-population is shown in brackets. The average of the mode obtained is also shown alongside with the mean PDI value. 45

Table 6. Summary of the results on the paper assay. 52

Acronyms

BCA	Bicinchoninic Acid
CBM	Carbohydrate-binding modules
CIP	Cellulosome-integrating protein A
DLS	Dynamic light scattering
HF	Hydrogen fluoride
LB	Luria-Bertani
LCPAS	Long-chain polyamines
SCH	Silica/cellulose hybrid
SEM	Scanning electron microscopy
SiNPs	Silica Nanoparticles
TCH	Titanium dioxide/cellulose hybrid
TEOS	Tetraethyl orthosilicate
Ti-BALDH	Titanium (IV) bis (ammonium lactato) dihydroxide
TiNPs	Titanium Nanoparticles
TMOS	Tetramethyl orthosilicate

1. Introduction

1.1. Nanoparticles

Nanotechnology is a "technology at the nanoscale", which produces novel materials and devices through the manipulation of matter at the atomic, molecular or macromolecular scale (Filipponi and Sutherlan, 2007; Prathna et al., 2010; Ramsden, 2011). Nanotechnology has been seen as crucial to scientific advancement in the 21st century, having contributed to developments/innovations in a wide variety of fields, such as agriculture, food, health, transportation, energy, and electronics resulting in a growth in the number of novel nanomaterials (Mangematin and Walsh, 2012; Grillo et al., 2015).

The most commonly studied nanomaterials are nanoparticles (Grillo et al., 2015). In general, nanoparticles are defined as particles with an average size between 1 and 100 nm; some of their properties are not found in bulk models with the same material (Auffan et al., 2009; Grillo et al., 2015). However, in the biological sciences, nanoparticles are defined as particles with a size smaller than 1000 nm. Their size is the key feature that allows them to preserve their unique physicochemical properties when compared to bulk materials (Buzea et al., 2007; Li et al., 2011). Nanoparticles can be classified according to their morphology - tubular, spherical, or irregular (Nowack and Bucheli, 2007). They can be divided into two groups: organic and inorganic (Prathna et al., 2010). Organic nanoparticles can be made of a variety of materials such as carbon (fullerenes and nanotubes), polymers (alginate, chitosan) and lipids (like soybean lecithin and stearic acid). Inorganic nanoparticles include several varieties of particles such as magnetic nanoparticles, noble-metal nanoparticles (l e.g. gold and silver), semiconductor (e.g. titanium dioxide and zinc oxide) and non-metal nanoparticles (e.g. silica and quantum dots) (Prathna et al., 2010; Grillo et al., 2015).

Nowadays, the interest in inorganic nanoparticles has been growing thanks to their distinctive electrical, optical, catalytic, and magnetic properties (Prathna et al., 2010). For example, the properties of silica nanoparticles (SiNPs) have been widely studied. SiNPs have been used in several applications thanks to their exceptional physicochemical, mechanical and optical properties (Rahman et al., 2009; Ding et al., 2012). SiNPs are being used not only in biomedical applications (e.g. drug delivery, cell markers), but also in different industries (e.g. insulators, electronic devices) due to characteristics such as biocompatibility, monodispersity, stability, high drug loading efficiency and their potential for hybridization with other materials, among others (Gholami et al., 2013; Tamba et al., 2015).

Another inorganic nanomaterial that is widely used is based on titanium dioxide nanoparticles (TiNPs) (Li et al., 2014a). This nanomaterial has been used as an additive agent in food and it works as a coloring agent that promotes opacity and whiteness in inks, as well as in personal care products (Li et al., 2014a). Furthermore, TiNPs have been commonly applied in sunscreens due to their optical properties, since they have a remarkable ultra violet (UV) absorbance, especially in UV-B (Smijs and Pavel, 2011; Li et al., 2014a).

1.2. Chemical and physical properties

1.2.1. Chemical and physical properties of SiNPs and their applications

Silicon is the second most abundant element in the earth's crust. Silicon is usually found together with other elements, such as oxygen, with which it forms silicate or silica (SiO_2) (Lechner and Becker, 2015). In nature, silicon is found in alkali feldspars, silicate minerals quartz and amorphous biogenic silica. Biosilica is the most abundant biogenic mineral in the Earth's crust produced by several living organisms such as higher plants, diatoms and sponges (Lechner and Becker, 2014, 2015). The production of biogenic silica is estimated to be about $240 \pm 40 \times 10^{12}$ mol of silicon per year in surface waters (Lechner, 2013).

Silicon dioxide, also designated as silica or silicon oxide, is a white compound that has a molecular weight of 56.96 g/mol, a density of 2.4 g/cm^3, a boiling point of 2230ºC, and a melting point of 1600ºC (AZoNano, 2013).

The surface of SiNPs is generally negatively charged, and composed by hydroxyl groups that are linked to silicon atoms, i.e. silanol groups (Yazdimamaghani et al., 2013).

As it is known, the physical and chemical properties of the particles change according to their size. In the case of SiNPs, Rahman et al. reported that their remarkable physicochemical and optical properties are the result of a decrease in size (Rahman et al., 2009). For example, through a photoluminescence analysis it was demonstrated that the enhancement of their optical properties thanks to an increase in the intensity of the blue (~2.32 eV) and green (~2.85 eV) bands is related to a decrease in size (Rahman et al., 2009). Based on these properties, and also on the nontoxicity and biocompatibility of SiNPs, Babu et al. developed an optical biosensor with high selectivity where they used a luminescent SiNPs-aptamer conjugate system for thrombin detection (Babu et al., 2013).

In addition to the properties already mentioned, the surface of SiNPs offers stability and is easily functionalized by covalent attachment or physical adsorption (Qhobosheane et al., 2001; Babu et al., 2013). For example, Wang et al. developed a laccase biosensor in which they used phytic acid functionalized SiNPs for the sensitive detection of the neurotransmitter dopamine (Wang et al., 2014). Schlipf et al. used two different ways to functionalize SiNPs: the functionalization with reactive titanium precursor (titanium (IV) ethoxide) or with decyl groups (using n-decyltriethoxysilane silane), with aim to measured flavonoid adsorption. This study revealed potential uses for functionalized SiNP platforms in the adsorption and recovery of natural compounds like flavonoids, which usually have anti-oxidant and anti-inflammatory properties (Schlipf et al., 2015).

Furthermore, SiNPs have been used for drug delivery purposes. For example, Niemelä et al. developed a drug delivery system based on glucose as an affinity ligand for decorated mesoporous SiNPs to deliver the drug celastrol, which induces apoptosis in cancer cells (Niemelä et al., 2015).

1.2.2. Chemical and physical properties of TiNPs and their applications

Titanium is the ninth most abundant element in earth's crust. However, it is not found in nature by itself, but together with others elements, such as oxygen (Shi et al., 2013) . Titanium compounds are found in minerals such as rutile (titanium oxide), ilmenite (iron titanium oxide), but also in living organisms, namely marine organisms such as diatom algae, which can have up to 1254 ppm of titanium in their cells walls (Cole et al., 2006; Buettner and Valentine, 2012).

Titanium dioxide (TiO_2), also known as titanium (IV) oxide (IV is the most common oxidation state) and titania, can present three different crystal structures: rutile, anatase and brookite (less common) (Zallen and Moret, 2006; Buettner and Valentine, 2012). This mineral is a white pigment and a semiconductor with a molecular weight of 79.9 g/mol. TiO_2 has a melting point of 1843 ºC, a boiling point of 2973 ºC, a relative density of 4.26 g/cm^3 at 25ºC, and a high refractive index (Shi et al., 2013).

As already mentioned, the use of titanium dioxide nanoparticles (TiNPs) has been explored in several fields, such as photocatalysis (Seyghali and Zanjanchi, 2015), sunscreens (Smijs and Pavel, 2011), tints (Zallen and Moret, 2006), and sensing devices (Song et al., 2006).

In photocatalysis, anatase is preferred over rutile, because it is more chemically reactive than the latter (Shi et al., 2013). As reported by Sayes et al., anatase TiNPs show a higher photoactivity, producing greater levels of reactive species under ultraviolet light than rutile TiNPs (Sayes et al., 2006). Photocatalysis is a promising method for the degradation of toxic pollutants in water, where TiO_2 NPs have been widely studied as catalysts (Seyghali and Zanjanchi, 2015). The photocatalytic activity of TiO_2 results from the fact that this compound is a semiconductor with a large intrinsic band gap (3.0 eV for rutile and 3.2 eV for anatase), which allows it to produce photo-generated charge carriers (electrons and holes) when it absorbs UV light (Xu et al., 2006; Seyghali and Zanjanchi, 2015) This phenomenon leads to the production of hydroxyl radicals, which are necessary for oxidating the organic compounds present in the water (Seyghali and Zanjanchi, 2015). Several applications of photocatalysis with TiNPs have already been developed. For example, Ling et al. developed a photocatalysis-based method for the degradation of phenol in water, in which they showed that TiNPs with a diameter of 10-23 nm generated via the sol-gel method produced a high concentration of hydroxyl radical that effectively removed phenol from water (Ling et al., 2015). On the other hand, Barndõk et al. developed a method of solar photocatalysis by using an immobilized nitrogen and fluorine co-doped titanium composite with monodisperse TiNPs that degrade 1,4-dioxane in wastewater (Barndõk et al., 2016) .

In the field of sensing devices, Li et al. used TiNPs to develop a novel nonenzymatic nitrite sensor (Li et al., 2014b), whereas Song et al. used TiNPs as an interface to enhance the detection sensitivity of biomolecular recognition events in some antitumor drugs, namely dacarbazine (Song et al., 2006).

1.3. Methods for SiNPs and TiNPs synthesis

1.3.1. Abiotic route for SiNPs/TiNPs synthesis

1.3.1.1. Sol-gel method

Sol-gel is a popular chemical method used to produce SiNPs and TiNPs (Rahman and Padavettan, 2012; Burger et al., 2015). The method involves the use of a precursor solution, which by chemical reactions can undergo transition from the sol to a gel (Owens et al., 2016). Sol is defined as a stable colloidal dispersion of solid particles suspended in a liquid, while gel is composed by an interconnected network of solid phase particles which form a continuous entity that expands in a liquid (Owens et al., 2016).

Both inorganic metals salts such as metal salt alkoxides can be used as precursors in sol-gel technology (Pierre, 1998; Rahman and Padavettan, 2012). Metal salts such as aluminium chloride, AlCl are defined by general formula M_mX_n, wherein M is a metal, X an anionic group and m and n are stoichiometric coefficients. On the otherside, metal alkoxides have general formula $M(OR)_n$, where the alkoxy group (OR) are bind to the metal, which result from the reaction between metal and an alcohol ROH(Pierre, 1998). Generally, the silicon alkoxides precursors used to produce SiNPs are tetraethylorthosilicate (TEOS) - $Si(OC_2H_5)_4$ and tetramethoxysilane (TMOS) - $Si(OCH_3)_4$, while the most common titanium alkoxide precursor used to produce TiNPS is titanium (IV) isopropoxide (TIP) - $Ti(OCH(CH_3)_2)_4$ (Rahman and Padavettan, 2012; Burger et al., 2015).

Generally, the chemical reactions of metal alkoxide are characterized by two main reactions: hydrolysis and condensation. During hydrolysis, the alkoxide groups (-OR) suffer nucleophilic attack by oxygen atoms of the water molecules, which result in the release of an alcohol moiety and consequently in the formation of metal hydroxide (1). Subsequently, condensation reactions occur wherby the hydroxyl groups (-OH) of the metal hydroxide react with either another hydroxyl group with release of water and formation of M-O-M covalent bonds (2) or with the alkoxide group, which leads to the formation of M-O-M and release of an alcohol (3) (Sanpo, 2014).

(1) $\equiv M - OR + H_2O \rightarrow \equiv M - O - H + ROH$

(2) $\equiv M - OH + HO - M \equiv \rightarrow \equiv M - O - M \equiv + H_2O \quad (\text{water condensation})$

(3) $\equiv M - OR + HO - M \equiv \rightarrow \equiv M - O - M \equiv + ROH \quad (\text{alcohol condensation})$

During the polycondensation reactions the particles will grow in size where the monomers turns to oligomers, trimmer until the final stage that form polymers (Branda, 2011).

Stable sols can be achieved in specific conditions that lead to produce nanoparticles (Branda, 2011). Silica sols with spherical particles of 0.05 µm to 2 µm obtained by sol-gel processes were first reported by Stöber et al. The method uses a silicon dioxide precursor such as TEOS, which is hydrolyzed and condensed to synthesize uniform silica particles in aqueous alcohol solutions (e.g. ethanol). This solution contains ammonia (NH_3), which is used as a morphological and basic catalyst. The authors observed that this catalyst is essential for synthesis of spherical silica particles since absence of

ammonia during the reaction resulted in silica flocculation in irregularly shaped particles (Stöber et al., 1968).

Based on Stöber method, other works have been described for the synthesis of silica particles and also for optimization of reaction parameters to obtain the size and morphology desired for silica particles which become the favored method for SiNPs production (Rahman and Padavettan, 2012; Lovingood et al., 2013). The Stöber method is simple process and yields monodispersed spherical nanoparticles when compared with acidic (e.g. HCl as catalyst) conditions, which produce gel structures (Rossi et al., 2005; Rahman and Padavettan, 2012). On the other hand, when the aim is the encapsulation of organic dyes, the basic components of Stöber synthesis can interfere with the chemistry of the dye, in contrast with bio-inspired routes of silica formation (e.g. diatoms) which can occur at neutral pH (Ducheyne et al., 2011)

The sol-gel method is also used to produce TiNPs. The process involves the hydrolysis and polycondensation reaction of a titanium alkoxide, such as titanium (IV) isopropoxide (TTIP) , in a solution of alcohol-water (Liu et al., 2011; Thangavelu et al., 2013). This method used acid as a catalyst, for example acetic acid (Zainizan Sahdan et al., 2012). If the aim is to obtain nanocystalline nanoparticles (e.g. anatase), the nanoparticles must be calcinated at high temperatures (e.g. 400 ºC) (Thangavelu et al., 2013).

1.3.1.2. Chemical vapor deposition

Chemical vapor deposition is another common method used to produce SiNPs and TiNPs (Zhang et al., 2013; Rezaei et al., 2014)

Generally, this technique uses titanium tetrachloride or titanium (IV) butoxide and silicon tetrachloride as precursors to produce TiNPS and SiNPs, respectively (Abdul Rashid et al., 2010; Zhang et al., 2013; Rezaei et al., 2014). Typically, the substrate where the solid product is deposited is exposed to vaporized precursors. In order to promote the reaction of the precursors is required some activation steps. Usually, the activation occurs at high temperature conditions in a flame reactor. During the deposition on the substrate surface, the reactants suffer nucleation and growth (Adachi et al., 2003; Rezaei et al., 2014)

Among these methods, there are other methods which are used to produce SiNPs and TiNPs such as water in oil micro-emulsion (Ping et al., 2006; Finnie et al., 2007) and hydrothermal synthesis (Akarsu et al., 2006; Gu et al., 2012).

1.3.2. Biomimetic approach based on diatom frustules

Over the last few years, biomimetic synthesis is being increasingly used in order to synthesize inorganic materials under ambient conditions (Ghosh et al., 2012).

Several studies have focused on the use of biomolecules, such as proteins, DNA, RNA and amino acids, which have the ability to control the nucleation and growth of nanomaterials at different stages (Ghosh et al., 2012). In particular, silica bio-mineralization in diatoms has inspired researchers for the biomimetic production of silica nanomaterials under *in vitro* conditions (Kröger et al., 2001). This biological mechanism proves to be must faster than abiotic formation for silica materials (Lechner, 2013).

1.3.2.1. Diatom algae

Diatoms are unicellular eukaryotic microalgae (about 1-500 µm in length) that belong to the class Bacillariophyceae (Parkinson and Gordon, 1999; Gordon et al., 2009; Dolatabadi and de la Guardia, 2011).These algae are ubiquitous organisms that correspond to the main group of phytoplankton in the oceans and they are responsible for about 20% of the global gross biological primary production (Lohman, 1960; Kröger, 2007). Their cell walls (known as frustules) are known to have intricate patterns made of amorphous silica in the nano- to micro-meter ranges (Parkinson and Gordon, 1999; Sumper and Kröger, 2004) (Figure 1).

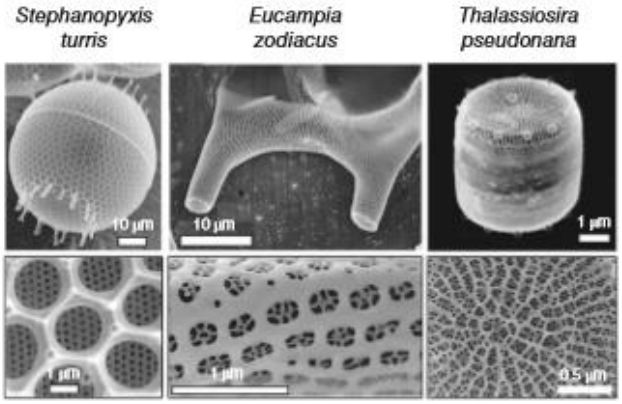

Figure 1. Electron microscopy images of cell wall structures from different diatom species. Species: Stephanopyxis turris, Eucampia zodiacus,Thalassiosira pseudonana(Kröger and Brunner, 2014).

There are over 100 000 different species of diatom, which are classified according to the wide variety of their frustules morphologies (Parkinson and Gordon, 1999; Dolatabadi and de la Guardia, 2011). In terms of symmetry, diatoms can be divided into two orders: centric and pinnate. Centric diatoms have radial symmetry, while pinnate diatoms have bilateral symmetry (Parkinson and Gordon, 1999; Dolatabadi and de la Guardia, 2011).

Diatom biosilica, an hybrid is formed by biomolecules that are firmly attached within amorphous hydrated silica (Sumper and Kröger, 2004). Some of these organic constituents of biosilica have been identified in different diatom species that are able to mediate and accelerate the synthesis of silica nanospheres *in vitro,* using a silicic acid solution under ambient conditions and neutral pH. These organic components are polypeptides known as silaffins and long-chain polyamines (LCPAs) (Kröger et al., 1999, 2000). LCPAs can be found as free molecules, but also covalently attached to the lysine residues of silaffins (Kröger et al., 2002; Jantschke et al., 2014).

The biomolecular self-assembly mechanism for silica formation as well as the variety and intricate silica micro nanostructures of the diatom are being increasingly used in nanotechnology applications, such as biomimetics, photonics, optics, biosensing, drug delivery, molecular separation, electronic and structural materials (Sumper and Kröger, 2004; Dolatabadi and de la Guardia, 2011; Kröger and Brunner, 2014).

1.3.2.2. Biosilicification in diatom cell cycle

Biosilicification is the production of silica by living organisms via the transfer of silicic acid to the organism and its conversion into silica (Otzen, 2012). Silicic acid or orthosilicic acid ($Si(OH_4)$), also known as monomeric silica, is the only soluble form of silica that living organisms are able to assimilate (Brümmer, 2003). This process occurs under mild physiological conditions and, therefore it does not need high pressure and temperature (Otzen, 2012).

The silica cell walls of diatom are composed of two similar halves: the epitheca (the larger one) and the hypotheca (the smaller one) which fit together like the two parts of a petri dish (Parkinson and Gordon, 1999; Kröger, 2007). Each theca comprises a valve and grilled bands, i.e. silica strips with porous pattern (Sumper and Kröger, 2004; Lechner and Becker, 2015).

During the cell division, diatoms need to synthesize a new silica cell wall. In this process, silicic acid is obtained from an aqueous habitant via the silicic acid transport proteins found in the protoplasm membrane (Kröger and Brunner, 2014). Then, biosilica formation is produced in a specific organelle known as the silica deposition vesicle (SDV), where the new valve is formed in minutes (Kröger et al., 1999).

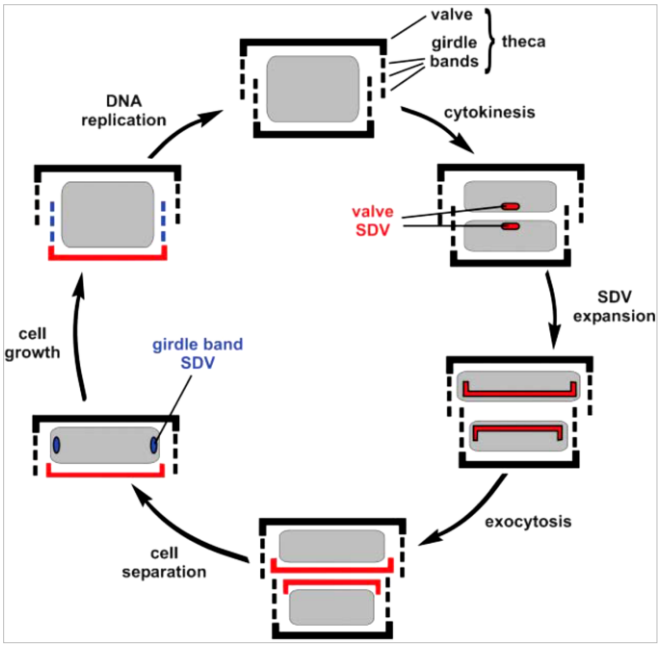

Figure 2. Biosynthesis in silica cell wall of diatoms (schematic). The cells are shown in cross-section. This scheme shows the different stages of the cell cycle. 1. The diatom cell has the maximum number of girdle bands; 2. Following cytokinesis, each sibling protoplast (grey) produces new biosilica (red) inside a valve SDV that gradually grows due to accumulation of silica; 3. Complete valve formation into SDV; 4. The complete valves are deposited on the diatom cell surface via exocytosis; 5. Separation of the sibling cells; 6. In order to expand the volume of the protoplast, new silica (blue) is formed within girdle band SDV; 7. During cell growth, several girdle bands are released to the lateral surface by exocytosis; a new cell division starts when the cell volume reaches its maximum. Figure taken from (Sumper and Kröger, 2004; Lechner and Becker, 2015).

During cell division of diatom, once mitosis and cytokinesis are completed, the two sibling cells synthesize an SDV valve in each in their protoplast (Figure 2). The SDV progressively grows due to the accumulation of precipitated silica until the newly formed valve is finished. Then, the complete valve is deposited on the diatom cell surface of each protoplast via exocytosis of the SDV and, consequently there is a separation of the sibling cells. Later on, during interphase several girdle bands are produced in individual SVDs and released gradually to the lateral surface of the cell in order to keep the protoplast closed, as well as, to enable the growth of the cell by increasing the distance between the two valves, epitheca and hypotheca (Sumper and Kröger, 2004; Lechner and Becker, 2015).

1.3.2.3. Organic constituents of diatom biosilica

The recognition of the organic constituents such as silaffins and LCPAs has been useful to find new bioinspired routes for the biomimetic synthesis of silica nanostructures at ambient conditions (Kröger et al., 2001; Patwardhan et al., 2003). Despite all the research focused on the biosilicification of diatoms, the process via which these biomolecules are able to turn an intricate and complex organic structure into a biological structure remains unclear (Otzen, 2012).

1.3.2.4. Silaffins proteins

Kröger et al. identified the proteins involved in diatom biosilicification (Kröger et al., 1999). They examined the cell wall from the *Cylindrotheca fusiformis* diatom via the solubilization of silica using anhydrous hydrogen fluoride (HF). The HF-extractable material showed that silaffin proteins were the most abundant protein constituent with high affinity to silica (around 4-17 kDA). Silaffin proteins are composed of three polypeptides: silaffin-1A (a mix of two similar peptides - silaffin-$1A_1$ and silaffin-$1A_2$), with approximately 4 kDa; silaffin-1B, with approximately 8 kDa, and silaffin-2, with approximately 17 kDa (Kröger et al., 1999, 2001).

Based on the sequence information of the silaffins found in *C. fusiforms* it was possible to identify a 795-base pair (bp) open reading frame, known as *sil1*, which encodes the precursor polypeptide si1p and contains 265 amino acids (Figure 3). The NH_2-terminal domain of sil1p contains a typical signal of 1 to 19 amino acid residues followed by an acidic peptide sequence of 20 to 107 amino acids whose function remains unknown (Kröger et al., 1999; Lechner and Becker, 2015). The basic COOH-terminal domain of sil1p is composed of seven extremely homologous repeating units (R1 to R7), which contain Lys-Lys (KK) and Arg-Arg (RR) clusters spaced according to a highly regular configuration. Between them there are predominant stretches of the hydroxyl-amino acids serine and tyrosine. The largest repeating unit is the R1 unit, which contains 33 amino acids; the second largest one is R2, composed of 22 amino acid residues; the shortest ones are the five units that range between R3 and R7, each of which contains 19 amino acid residues (Figure 3) (Kröger et al., 1999).

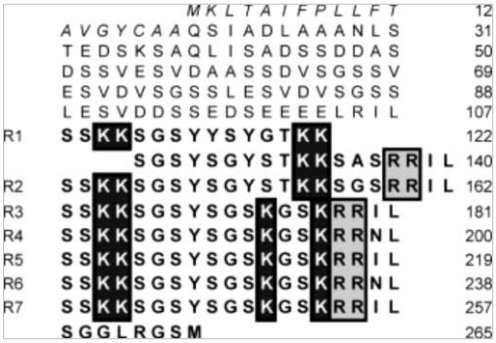

Figure 3. The amino acids sequence of polypeptide sil1p. Italic letters (residues 1 to 19 residues) represent the typical signal sequence followed by a peptide sequence (residues 20 to 107) that contain a large amount of acidic residues. The COOH-terminal domain is represented by bold letters with boxed lysine residues and arginine. R1 to R7 are the seven homologous repeating unit amino acids (Kröger et al., 1999). A, Ala; C, Cys; D, Asp; E, Glu; F, Phe; G, Gly; I, Ile; K, Lys; L, Leu; M, Met; N, Asn; Q, Gln; R, Arg; S, Ser; T, Thr; V, Val; and Y, Tyr. Figure taken from (Kröger et al., 1999).

Both silaffin-1A and -B are obtained via the endoproteolytic processing of sil1p, where each repeat unit (R1 to R7) correspond to an individual peptide. Silaffin-$1A_1$ is derived from repeating units R3 to R7, silaffin-$1A_2$ is derived from repeating unit R2, while silaffin-1B is derived from repeating unit R1 (Kröger et al., 2001). Mature silaffin peptides do not contain the four COOH-terminal amino acid - RRIL or RRNL - predicted by the gene sequence of *sil1.* During the maturation of the precursor silaffin protein sil1p,

these patterns (RRIL and RRNL) found in each repeat unit are cleaved off or subject to post-translational modifications (Kröger et al., 2001).

In order to complete the chemical structure of silaffins, the preferred method consists of a gentle extraction based on an aqueous solution of ammonium fluoride that preserves *in vivo* silaffin structures, instead of the HF extraction, which does not preserve post-translational modifications (Figure 4). The biochemical analysis of the silaffins obtained via this gentle extraction method reveals their complete chemical structure, which presents several post-translational modifications. The native silaffin-$1A_1$ (natSil-$1A_1$) contains all their lysine residues with modifications post-translational, which result: ε-N,N-dimethyllysine, phosphorylatede ε-N,N,N-trimethyl-δ-hydroxylysine and derivatives of polypropylenimine (six to eleven units). Furthermore, natSil-$1A_1$ has eight phosphate groups where seven of them bind to all seven serine residues and the other binds to a trimethyl-δ-hydroxylysine (Kröger et al., 2001, 2002; Sumper and Kröger, 2004).

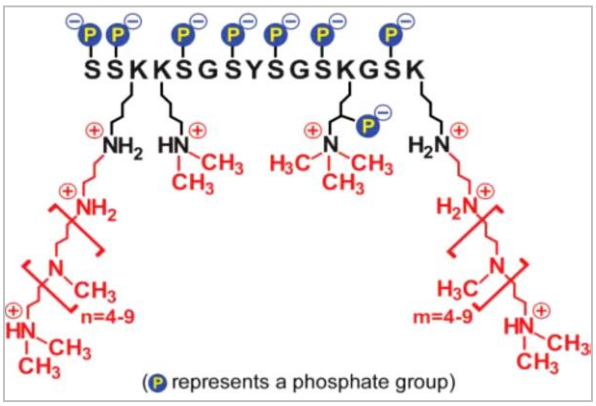

Figure 4. Chemical structure of NaSil-1A1. The charge represented is an attempt for the solution with pH=5. Post-translational modifications of lysine residues: oligo-N-methy-propylamine (K15 and K3), ε-N,N-dimethyllysine (K4), phosphorylated ε-N,N,N-trimethyl-δ-hydroxylysine (K12). All of the serine residues are phosphorylated.). A, Ala; C, Cys; D, Asp; E, Glu; F, Phe; G, Gly; I, Ile; K, Lys; L, Leu; M, Met; N, Asn; Q, Gln; R, Arg; S, Ser; T, Thr; V, Val; and Y, Tyr. Figure taken from (Sumper and Kröger, 2004).

Kröger et al. tested the dependence of phosphate groups for the silica precipitation activity by replacing the phosphate buffer with a sodium acetate buffer. The results revealed that polycationic silaffin-1A (peptide obtained with HF extraction) did not promote silica precipitation, while NatSil-1A induced silica precipitation from silicic acid solution (pH 5.5) within just few minutes, forming nanospheres with diameters ranging between 400 nm and 700 nm. This result proved that phosphorylation is crucial for biological activity (Kröger et al., 2002).

Furthermore, the polyamine modifications of lysine residues have proven to be important for silica precipitation activity at pH values below 7 by accelerating this process (Kröger et al., 1999). Comparing the silica precipitation activities of silaffin-A and synthetic silaffin peptide R5 at different pH values revealed that silaffin-A is able to promote silica precipitation within seconds at pH values below 7, showing its maximal activity at pH values around 5; this makes sense because biosilicification in diatoms occurs in an acidic environment in the SDV. However, synthetic R5 with the amino acid sequence of

repeat unit R5 that do not present amino acid modifications are incapable of precipitating silica at pH values below 6. This result indicates that the modification of lysine residues with longer polyamine residues may be are important for inducing silica precipitation under physiological conditions. (Kröger et al., 1999).

The most interesting result was the fact that silica nanospheres (400 nm to 700 nm in diameter) generated by nat-Sil-1A *in vitro* by using pre-hydrolyzed TMOS as precursor do not correspond to the size of the particles that formed the diatom biosilica, whose spheres have 10 to 100 nm in diameter, possibly due to the different conditions provided by the *in vivo* and *in vitro* studies (Kröger et al., 2002).

Silaffin-2 is another protein associated with silicified cell walls. This protein is not encoded by the *sil1* gene, unlike silaffin-1A and 1B. As other silaffins, native silaffin-2 (natSil-2) is also highly post-translational, but it has a high negative density due to the presence of numerous glucuronic acid and carbohydrate modifications. In contrast with natSil-1A, natSil-2 decreases its silica precipitation activity *in vitro*. However, when this protein is mixed with natSil-1A or LCPAs it regulates their activities under phosphate-free conditions. In different ratios, both proteins generate macroporous silica particles ranging between 100-1000 nm with different morphologies. It has been suggested that this structure might be generated due to the self-assembly mechanism developed by an organic matrix, which involves electrostatic interactions between the different biomolecules that allow forming porous biosilica patterns (Poulsen et al., 2003).

1.3.2.5. Model for silica precipitation by silaffins

There are several methodologies for the creation of new materials that involve the use of organic molecules as templates in order to produce inorganic structures such as TiO_2 and SiO_2 (van Bommel et al., 2003).

The chemistry of the silica formation involves the polymerization of the monomeric silicic acid ($SiOH_4$) through the condensation reactions of silanol groups (Si-OH) to siloxane bond (Si-O-Si) in order to form dimers, trimers and cyclic oligomers, which further polymerize so that the siloxane bonds are maximized, creating highly dense, branched polysilicic acid species. Additionally, these species continuous to grow by polymerization processes or via the fusion of particles, which result in creation and growth of spherical particles (Sumper and Kröger, 2004). Depending on conditions such pH and the presence of the salts or additive, the colloidal silica particles can remain as a sol, can form a gel or can be induced to precipitate (Figure 5). If the pH is below 7, the weak electrostatic repulsion dominates due the uncharged surface of the silica particles, which lead to aggregation and formation of a rigid three-dimensional network called gel. If the pH is above 7, sol is stable due the domination of negative charges on the surface of the colloidal particles which promote electrostatic repulsion between the particles. However, silica sol can become unstable when a flocculating agent is added to the system, leading to the precipitation of particles (Lechner and Becker, 2015). Precipitation is the formation of separate and

dense aggregates of particles through flocculation; these aggregates are densely packed and generate the hard silica found in the diatom frustule (Pierre, 1998; Sumper and Kröger, 2004). Silaffin proteins can be seen as a biological flocculating agent, because they promote and accelerate silica precipitation (Sumper and Kröger, 2004; Lechner and Becker, 2015).

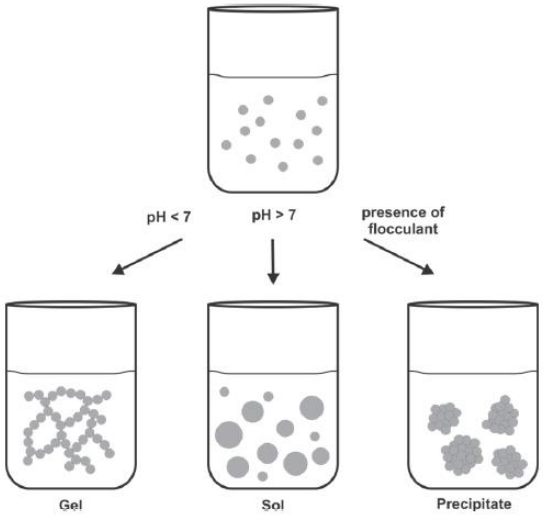

Figure 5. Chemistry of silica. Formation of a sol when pH is above 7, formation a gel when pH is below 7 and precipitation of the colloidal silica particles when a flocculant is added. Figure taken from (Lechner and Becker, 2015).

It has been suggested that the self-assembly of silaffins is required for silica formation, because the resulting assemblies provide a silaffin-based template for silicic acid polycondensations. Native silaffins have a zwitterionic structure that results from polyamine modifications and a high level of phosphorylation that allows self-assembly to occur via electrostatic interactions. On the other hand, the structure of polycationic silaffins does not contain phosphate groups and, therefore, they can only induce silica precipitation through the addition of phosphate anions to the solutions. Most likely, phosphate anions act as cross-linkers that promote the aggregation of polycationic silaffins and, consequently, the self-assembly mechanism (Kröger et al., 2002).

Furthermore, synthetic polyamine molecules such as polyallyalamine and poly-l-lysin can induce silica precipitation, suggesting that the silaffins contained in their amino groups work as an acid-base catalyst that enables the formation of the siloxane bond (condensation reactions) (Kröger et al., 2000; Lechner and Becker, 2015) (Figure 6). The amino group which act as base, is a deprotonated group ($-NH_2$) and so accepts a proton from a silicic acid molecule which leads to the formation of a reactive silanolate group $\equiv SiO^-$. This group generates a nucleophilic attack to a second silicic molecule. In order to facilitate this attack, the amino group acts as acid (($-NH_3^+$) protonated group) promoting the release of a water molecule from the attacked molecule through protonation (Kröger et al., 2000; Lechner and Becker, 2015).

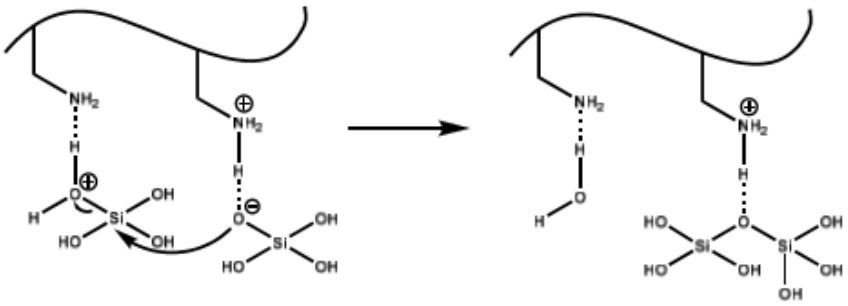

Figure 6. Proposed mechanism for silaffin peptide-mediated poly-condensation reaction of silicic acid through its polyamine groups (Lechner and Becker, 2015).

Despite the fact that polyamine modifications have proven to be essential for the precipitation activity of native silaffins, the synthetic R5 does not contain post-translational modifications in its amino acids, while showing precipitation activity at pH values above 7 (Kröger et al., 1999, 2002).

1.3.2.6. Biomimetic templates based on biosilicification diatom algae

The methods used for the synthesis of SiNPs and TiNPs generally require extreme values of pH, temperatures and pressures (Sewell and Wright, 2006; Otzen, 2012). For example, the Stöber method requires high ammonia content and high pH to produce SiNPs (Stöber et al., 1968); whereas chemical vapor deposition processes use high temperatures and pressures (Rezaei et al., 2014).

The biosilicification process of diatom algae offer an alternative to produce nanomaterials at mildly acidic to neutral pH under ambient conditions (Patwardhan et al., 2007).This process probably involves silaffins self-assembles that act as template/scaffold for silicic acid polycondensation (Lechner and Becker, 2015).

Biomimetic inorganic material precipitation approaches have been developed in order to mimic the nature mechanism of precipitation through the use of synthetic analogues of biosilica organic constituents (Patwardhan et al., 2005; Cole et al., 2006).

Several synthetic biomolecules have been used to promote silica precipitation *in vitro*. For example, cationic polyelectrolytes through their positive charge can interact electrostatically with silica species (negatively charged), promote aggregation of silica and consequently phase separation (Patwardhan et al., 2005). Patwardhan et al. have tested a large range of cationic polymers, which include poly(allylamine hydrochloride) (Patwardhan and Clarson, 2002b), poly-L-arginine (Patwardhan and Clarson, 2003), poly-L-lysine (Patwardhan et al., 2001), polyethyleneimine (Patwardhan and Clarson, 2002a). TMOS has been preferred as a silica precursor since it hydrolysis faster when compared to the alternative TEOS (Patwardhan et al., 2001).

In addition to silica precipitation, the cationic polymer poly-L-lysine has also the ability to produce titanium oxide from the precursor titanium(IV) bis(ammonium lactato)-dihydroxide (Ti-BALDH) (Sewell and Wright, 2006).

The silica and titanium dioxide precipitating activity of the synthetic R5 has already been reported. It offers an advantage over polymers due to the possibility of recombining R5 with other proteins, for example to drive their encapsulation into a silica matrix (Sewell and Wright, 2006; Lechner and Becker, 2014).

1.3.2.7. The role of synthetic R5 peptide

The 19-amino acid-long synthetic R5 (SSKKSGSYSGSKGSKRRIL) is a biomimetic analog of the repeat unit R5 of the C-terminal part of polypeptide silp1 (Figure 3) of *C. fusiformis,* which lacks post-translational modification at its lysine residues. This peptide has silica precipitation activity in the neutral and alkaline pH range, while the maximum silica precipitation activity of silaffin-1A occurs at pH values of around 5 (Kröger et al., 1999).

The functional-sequence of the R5 has allowed understanding its unique silica precipitation abilities (Knecht and Wright, 2003; Lechner and Becker, 2014). The tetra amino acid motif (RRIL) present in the sequence of the R5 , is not found in the amino acid sequence of native silaffins that have been isolated from diatoms, indicating that this motif was proteolytically removed during the processing of the silaffin precursor polypeptide (Kröger et al., 2001). However, the experiment accomplished by Knecht and Wright reveals that the functions of the C-terminal RRIL motif are essential for the supramolecular self-assembled structure of the R5, working as template for silica precipitation (Knecht and Wright, 2003). The RRIL motif is constituted by two basic residues of arginine (RR), and two hydrophobic residues - isoleucine residue (I) and leucine residue (L).

Lechner and Becher also analyzed the silica precipitating activity of the R5 (Lechner and Becker, 2014). This study was focused on a series of peptide variants derived from the R5. The results of the mutations revealed that the localization of the RRIL motif (C-terminal, N-terminal or center) influenced the morphology of the resulting silica precipitated material, indicating that this motif is involved in the self-assembly of the peptide. Additionally, the RRIL motif is important for silica precipitation activity because R5 variants where arginine residues where replaced by other residues display no silica precipitation activity. This shows that the arginine guanidine groups present in the motif play a critical role in silica precipitation (Knecht and Wright, 2003; Lechner and Becker, 2014).

The authors suggest that the self-assembly of the R5 occurs via the salt bridges formed between the positively charged guanidine groups from arginine and the negatively charged phosphate anions from the buffer (Lechner and Becker, 2014). As in the R5, the self-assembly of native silaffins is also due electrostatic interactions driven by their oppositely charged posttranslational modifications (polyamine moieties and phosphate groups) (Kröger et al., 1999, 2002). However, the integration of

phosphoserine residues into the R5 appeared to inhibit its silica precipitation, but buffer phosphate is required to induce its self-assembly (Senior et al., 2015).

Furthermore, the number and the position of lysine residues in the sequence of the peptide, the chemical nature of neighboring amino acids and their charge showed to influence the silica material morphology. Spherical silica nanoparticles were obtained with the R5 sequence which has adjacent lysine residues but not with mutants, that have their lysine residues separated (Lechner and Becker, 2014). Additionally, it has been confirmed that the lysine residues found in the unmodified R5 are crucial for its silica precipitation activity, because the R5 variants in which all the lysine residues (Figure 7) were replace by alanine did not show any silica precipitation activity (Lechner and Becker, 2014).

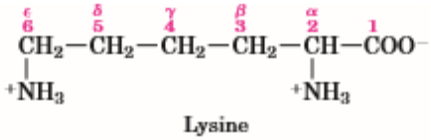

Figure 7. The structural formula of lysine amino acid at pH 7. Figure taken from (Nelson and Cox, 2004).

It has been suggested that the presence of the positively charged ε-amino groups of the lysine residues (Figure 8) in the R5 sequence mediated silica polycondensation that, in native silaffins, occurs due to the presence of long-chain polyamines linked to the ε-amino groups of the lysine residues (Kröger et al., 1999, 2002; Lechner and Becker, 2014).

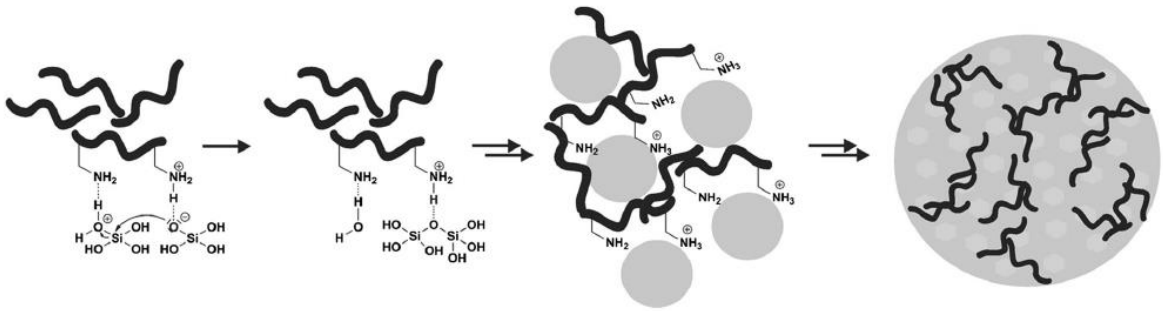

Figure 8. The proposed model for silica precipitation mediated by R5 peptide. Figure taken from (Lechner and Becker, 2014).

Senior et al. studied the structure of the R5 and its silicification ability. The concentration of silicic acid appeared to have a linear relationship with silica precipitation, but the concentration of the peptide and the pH are also parameters that should be taken into account. Silica precipitation only occurs above 1 mM of R5 at pH 7 and 8, while no rapid precipitation occurs at pH 6 for any peptide concentrations, confirming that pH is a critical parameter for the activity of the R5 (Figure 9) (Senior et al., 2015). Figure 9 shows that the precipitation seemed to have a cooperative behavior (sigmoidal behavior) with the peptide concentration.

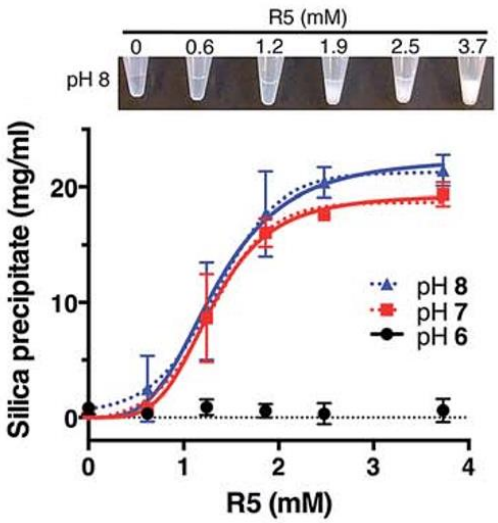

Figure 9. Silica precipitation as a function of R5 concentration and pH. All experiments used 50 mM silicic acid. Figure taken from (Senior et al., 2015).

Concerning about the structure of the R5, this peptide appears do not form any stable secondary structure and does not seem to assemble into peptide aggregates in solution. The results of the NMR (Nuclear Magnetic Resonance) and DC (Circular Dichroism) analyses indicate that the peptide exhibit to be a monomeric random coil in solution, which was exhibited at all pH values tested between 4.5 to 8.0. Moreover, the addition of silicic acid in solution did not induce the structural change in the R5 (Senior et al., 2015). This results do not support the spontaneously peptide self-assemble aggregates that appear to be necessary for silicification process (Knecht and Wright, 2003).

The experiments in which the R5 is used as a flocculating agent have resulted in amorphous silica material with different morphologies. Silica nanospheres are the most common specimen obtained *in vitro* under static conditions, both via the R5 and via native silaffins (Kröger et al., 2002; Knecht and Wright, 2003; Senior et al., 2015). However, the morphology of this material is influenced by the conditions of the reactions, as well as by the structure and chemical behavior of the flocculating agent (Lechner and Becker, 2015). Different silica structures can be obtained by using the R5 as a silica precipitating agent through a reaction based on physical changes and not on the static conditions that produce spherical silica. For example, bubbling nitrogen gas through the reaction mixture (R5 and TMOS) allowed obtaining arch-shaped structures, while applying mechanical shear to the reaction allowed obtaining fibrillary structures (Naik et al., 2003). Also, the addition of certain additives to the reaction mixture can influence the morphology of the silica structures. In the presence of hydroxyl groups from additives such as glycerol or sucrose, the R5 formed sheet-like silica structures (Rodríguez et al., 2004).

Diatom frustules are known to be intricate structures made of amorphous silica, but in addition to this constituent, these structures can also contain titanium in their natural habitat (Cole et al., 2006). Having this knowledge, the R5 precipitating activity was tested for this metal oxide. Pender et al. showed

that the R5 had the ability to precipitate silica and titanium oxide when they used its precipitating capacity to coat carbon nanotubes (Pender et al., 2006).

The ability of the R5 to form TiNPs has also been studied. Sewell and Wright reported the precipitation of amorphous TiNPs from a non-natural precursor of titanium (IV) bis(ammonio lactate) dihydroxide (Ti-BALDH, $[CH_3CH(O^-)CO_2NH_4]2Ti(OH)_2$) via the R5 at ambient conditions (Sewell and Wright, 2006). Like silica precipitation, titanium dioxide precipitation also proved to have a cooperative behavior in a peptide concentration at pH 7.5 (Sewell and Wright, 2006; Senior et al., 2015). Furthermore, Sewell and Wright reported that the R5 has a specific peptide activity for the titanium dioxide precipitation comparable (2.2 ± 0.2 nmol of titanium per min.nmol peptide) to the silica activity (3.59 ± 0.16 nmol silica per min.nmol peptide)(Knecht and Wright, 2003; Sewell and Wright, 2006). The R5 appeared to reach the maximum activity in the production of titanium oxide at pH values between 6 and 7.5. Moreover, the R5 peptide can induce titanium dioxide precipitation at absence of phosphate ions, in contrast with the mechanism of silica precipitation wherein the peptide required ions phosphates (Kröger et al., 2002; Sewell and Wright, 2006).

Like other groups of researchers (Knecht and Wright, 2003; Lechner and Becker, 2014), Wright and Sewell resorted to the use of variants of the R5 sequence in order to evaluate the role played by this peptide in titanium oxide precipitation. The results revealed that the variant without the RRIL motif showed inactive titanium dioxide precipitation activity, indicating that the RRIL motif is required for the self-assembled peptide structure as well as for silica precipitation (Knecht and Wright, 2003; Sewell and Wright, 2006; Lechner and Becker, 2014). They suggest that the self-assembly of the peptide allows creating a high local concentration of amino groups that interact with anionic Ti-BALDH precursor molecules and promote their condensation, in a process similar to the mechanism that promotes silica precipitation via the R5 (Sewell and Wright, 2006; Lechner and Becker, 2014).

Cole et al. tested Ti tris(citrate) and Ti-BALDH as titanium precursors and, in this case, the R5 proved to promote the rapid precipitation of oxide titanium from each previous precursor. However, the Ti-BALD is more suitable to be used as a precursor than Ti tris(citrate), because Ti-BALDH can be dissolved at high concentrations and it is easier to hydrolyze (Cole et al., 2006).

The titanium oxide formed by R5 is an amorphous material but, via the annealing process - which promotes its transition to the crystalline anatase phase as observed at 600ºC - and with an increase of temperature, it can be turned into rutile (Sewell and Wright, 2006).

1.4. Applications of R5

The functionalities of R5 peptide have been explored for different bio-inspire purposes, some of them are described below.

The fabrication of nanoparticle networks was achieved by using self-assembling R5 as a template. Jakhmola et al. reported the fabrication of non-spherical Pd (palladium) nanostructures using the peptide

scaffold (Jakhmola et al., 2010). They produced different Pd morphologies by controlling the Pd:peptide ratio, ranging from nanoparticles and nanoribbons to nanoparticle networks. So, the self-assembling peptides form a supramolecular structure that acts as template, allowing the amine moieties to bind Pd^{2+} ions. In addition to Pd nanoparticle networks, R5 were also used to fabricate Au (gold) nanoparticle networks at ambient temperature reported by Bhandari and Knecht (Bhandari and Knecht, 2012). The Au networks showed to be highly branched linear structures, reactive when compared to similar structures. The development of Pd, as well as Au nanostructures is relevant due to their catalytic applications, in which the use of the R5 as a biomimetic template proves to be a potential and functional method of producing new nanostructures.

R5 has also used been used to encapsulate esterases and lipases inside SiNPs. This was achieved by recombining R5 with the protein to be encapsulated. The results revealed that this kind of encapsulation afforded high yields of active entrapped protein, showing that it is a promising method for future applications in the industrial biocatalysis field (Emond et al., 2012). Choi et al. constructed an electrochemical biosensor for determining glucose concentrations. For this purpose, they started with the genetic fusion of R5 and glucose oxidase in order to immobilize the glucose oxidase enzyme into biomimetic SiNPs on a graphite rod electrode (Choi et al., 2011). Edwards et al. 2011 also obtained successful results when they used the peptide in order to encapsulate the human carboxylesterase 1 enzyme (associated with drug metabolism) into biomimetic SiNPs catalyzed by the R5. Unlike the formers, they did not resort to a genetic fusion of the R5 with the target protein (Edwards et al., 2013).

Beyond these applications, the abilities of the peptide were also used in the development of a hybrid organic and inorganic ordered nanostructure of SiNPs through the integration of the R5 into a polymer hologram, which is fabricated via a two-photon-induced photopolymerization. This nanostructure, combining the qualities of the two materials, enhances the processability of an organic polymer with the optical and mechanical properties of silica (inorganic), proving to be more efficient than a polymer hologram without silica and, therefore, to have a potential for the development of photonic devices (Brott et al., 2001). Pender et al. created a single-wall carbon nanotube composite by using the peptide to coat the carbon nanotube with titanium dioxide and silica. Carbon nanotubes have been used in electronics and sensors fields, and it could be interesting to pursue this biomimetic method because it avoids the use of high temperatures and/or harsh chemicals (Pender et al., 2006).

The silaffin R5 has been continuously used in cases studies, due to its self-assembly properties and to the ability to synthesize metal oxides.

1.5. Hybrid organic-inorganic composites

Composite materials are a combination of two or more chemically different materials that developed a continuous phase, such as polymer with a dispersed phase, namely silica, carbon particles, etc.

(Raman et al., 2012). These materials have unique properties, different from the ones of their original components taken separately (Raman et al., 2012).

Over the last decade, the development of organic-inorganic hybrid materials has become an interesting subject due to the interesting physicochemical properties that turn them into effective materials for an extensive range of applications (Raman et al., 2012). The unique properties of hybrid materials are a result, not only of the sum of the individual contributions of their components, but also of the generation of synergistic functions between organic and inorganic matters (Kimx et al., 2015).

The development of hybrid materials is mainly focused on the following objectives: the combination of different materials, the development of new synthesis methods and the functionalization of their materials (Guizard et al., 2001). Thanks to their properties, these materials have a great potential for a wide variety of applications in the area of advanced technologies, such as structural materials that comprise a matrix for high-performance composites and functional materials including sensors, catalytic supports and active glass. (Guizard et al., 2001; Messori et al., 2002; Castelvetro and De Vita, 2004).

1.5.1. Silica/cellulose and titanium dioxide/cellulose hybrid composite

Cellulose is a natural, linear polymer of β-(1→4)-D-glucopyranose that stands out as an abundant, easily available and renewable resource, chosen for diverse applications for its affordability (Taha et al., 2012; Demilecamps et al., 2014; Keshk et al., 2015). Generally, its structure comprises networks of intra- and inter-molecular hydrogen bonds with hydrophilic and mechanical properties (Yu et al., 2008) Cellulose shows several interesting characteristics, such as biocompatibility, mechanical strength, and a high chemical durability due to its strong intra- and inter-molecular hydrogen bonds (Svensson et al., 2005; Jia et al., 2011).

Several silica/cellulose hybrid (SCH) composites have been created in order to allow taking advantage of the combined properties of the two materials in a single system. There are various silica/cellulose composites, which are obtained using different types of cellulose and different synthesis methods.

For example, Xie at al. developed an SCH material with an improved thermal stability by using a crosslinking agent during the sol-gel process (Xie et al., 2009). Sequeira et al. produced SCH composites using two different methods: one based on the use of bleached *Eucalyptus glubulus* kraft pulp, and the other one based on the use of primary treatment sludge cellulose fibers by sol-gel, resorting to TMOS or TMOS/TEOS as precursors. Then, the hybrid material was aged using the hot pressing method. Silica showed to improve cellulose by increase its stability while soaked in water, hydrophobicity, and thermal stability (Sequeira et al., 2009).

Taha et al. developed a functionalized cellulose acetate/silica composite nanofibrous membrane in order to remove the Cr(VI) ion from aqueous solutions (Taha et al., 2012). This composite was prepared using the sol-gel method (with TEOS as silica precursor) combined with electrospinning. The resulting

composite had a high surface area and a high porosity (Taha et al., 2012). On the other hand, Naghsh et al. made a cellulose acetate/silica membrane for separating ethylene/ethane and propylene/propane (Naghsh et al., 2012). The membrane was prepared using the solution casting and solvent evaporation methods. The nanocomposite membranes were obtained by mixing the silica sol (TEOS as precursor) and the cellulose acetate solution in dimethylformamide (Naghsh et al., 2012)

The interest in titanium dioxide/cellulose hybrid (TCH) composites has also been increasing due their potential applications (Yu et al., 2008)

Uddin et al. created photoactive titanium oxide films on cellulose fibers using the sol-gel method. The film was made of anatase TiNPs that showed a photocatalytic activity (Uddin et al., 2007).

TCH composites can be also be used as antibacterial agents. Daoud et al. developed an antibacterial surface made of TiNPs on cellulose fibers using the sol-gel method, resorting to titanium tetraisopropoxide as precursor of TiNPs in acidic water (Daoud et al., 2005).

TCH composites have proven to be interesting materials for biosensing applications. Abdullahi et al. reported the use of a TCH in the composition of a disposable urea biosensor. The composite was produced by combining TiNPs with a cellulose solution. The enzyme urease was entrapped in the THC through physical adsorption. This biosensor proved to be highly sensitive (Abdullahil et al., 2015). Furthermore, Maniruzzaman et al. developed a TCH nanocomposite for immobilizing glucose oxidase through physical adsorption, in order to create a conductometric glucose biosensor. This biosensor also proved to be sensitive (Maniruzzaman et al., 2012).

1.6. Carbohydrate-binding modules

Glycoside hydrolases, such as cellulases and hemicellulases, are carbohydrate-active enzymes that are specifically and tightly associated to their insoluble substrates (e.g. cellulose and hemicellulose) in order to promote their degradation via the hydrolysis of the glycosidic bonds (Tomme et al., 1996; Arfi et al., 2014). Structurally, glycoside hydrolases, consist of a catalytic module and one or more carbohydrate-binding modules (CBM) (Hashimoto, 2006). The CBM plays an important role in the enhancement of the enzymes' activity by promoting their binding to the carbohydrate substrate and increasing the concentration of enzymes on the surface substrate (Bolam et al., 1998; Arfi et al., 2014). A CBM is a continuous sequence of amino acid residues contained in the carbohydrate-active enzyme with a discreet fold (Shoseyov et al., 2006). CBMs are commonly found in the N- or C-terminal of the parental protein, and less frequently found in a central position within the polypeptide chain, containing between 30 and 200 amino acids (Shoseyov et al., 2006).

Currently, the "Carbohydrate-Active Enzymes" database (CAZy - http://www.cazy.org) divides CBMs into 74 families according to their similarities in terms of amino acid sequence, binding specificity and structure (Shoseyov et al., 2006). In this classification, CBMs are also divided into "fold families",

which are defined according to their protein fold and tridimensional structure (Boraston et al., 2004). In terms of the number of families, the predominant fold is the β-sandwich form, being the second most common fold the β-trefoil form (Boraston et al., 2004; Oliveira et al., 2015).

Additionally, CBMs are divided into three types according to their function: type A ("surface-binding" CBMs), type B ("glycan-chain-binding" CBMs) and type C ("small-sugar-binding" CBMs) (Oliveira et al., 2015).

Type-A CBMs are characterized for their ability to bind to insoluble, highly crystalline cellulose and/or chitin. The fact that they can bind to the substrate may be related to the aromatic amino acids in the binding sites. These CBM binding sites have a planar architecture that is complementary to the surfaces present in cellulose or chitin crystals. CBMs in this group appear to have a low affinity, or no affinity at all, for soluble carbohydrates (Boraston et al., 2004; Hashimoto, 2006).

Type-B CBMs seem to depend on the carbohydrate ligand polymerization degree. For example, they appear to have a high affinity for hexasaccharides, but they also have an insignificant interaction with oligosaccharides of a lower polymerization degree. The architecture of their binding sites has grooves or clefts and comprises several subsites that are able to accommodate the individual sugar units of the polymeric ligand. As in Type-A CBMs, the aromatic amino acids play an important role in ligand binding and their orientation is crucial in terms of specificity (Boraston et al., 2004; Oliveira et al., 2015).

Finally, type-C CBMs have a lectin-like property, which consists in an optimal binding to mono-, di- or tri-saccharides; however, they do not have the extended binding site grooves found in type-B CBMs (Boraston et al., 2004; Hashimoto, 2006)

1.6.1. Cellulose-binding module family 3

The anaerobic bacterium *Clostridium thermocellum* is able to degrade insoluble cellulose by using a highly effective cellulosome, which is an extracellular multienzyme cellulolytic system attached to the cell wall of the bacterium (Figure 10). This system allows the conversion of plant-derived polysaccharides to soluble sugars and fermentation products. The cellulosome is composed by (hemi-)cellulolytic enzymes (catalytic subunits) and the noncatalytic polypeptide known as scaffoldin CipA (cellulosome-integrating protein A), which comprises nine cohesion domains and the CBM subfamily 3a. Cohesins only allow integrating nine catalytic subunits at a time, being mediated by the dockerin domain that binds to the catalytic subunits. The cohesin-dockerin interaction binds to the cell surface via the X module, whose function remains unknown. The CipA CBM3 in *C. thermocellum* (CBM3a), which is located between cohesin 2 and cohesin 3, plays a crucial rule by allowing the whole cellulosome enzyme complex to bind to the cellulosic substrate (Schwarz et al., 2004; Yaniv et al., 2013, 2014). In terms of function, CBM3 from *C. thermocellum* fits into Type A, but in terms of fold it fits into the β-sandwich family (Oliveira et al., 2015).

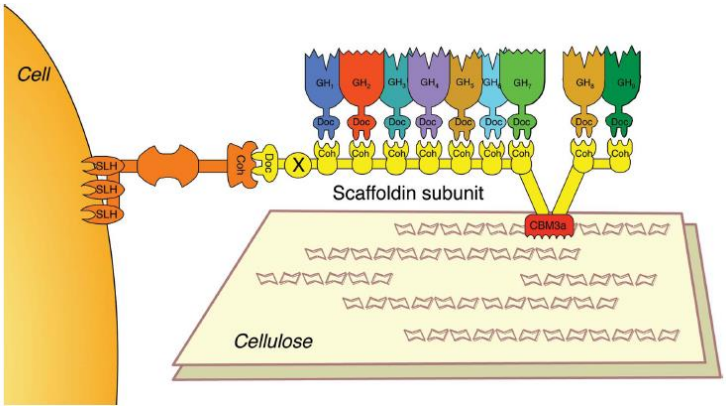

Figure 10. Schematic representation of the C. thermocellum cellulosome. The cbm3a is connected to the substrate cellulose and to two cohesins (Coh). There are nine highly homologous Coh modules binding to dockerin (Doc) modules, which can interact with the 70 possible glycoside hydrolases (GHs) into the cellulosome. The cellulosome is attached to the cell wall via a surface layer homology (SLH)-like module of an anchoring scaffolding. Figure taken from (Yaniv et al., 2013).

Tormo et al. analyzed the crystal structure of the CBM3 from the *C. thermocellum* CipA (PDB entry 1nbc), which comprises 155 amino acid residues. The CBM3 forms an antiparallel β-sandwich composed of nine β strands arranged as two antiparallel sheets with a Ca^{2+} ion that stabilizes that fold (Tormo et al., 1996; Yaniv et al., 2013). In Figure 11 we can see a ribbon diagram of CBM3 that showing the so-called bottom strands (1,2,7 and 4) and top (strands 9,8,3,6 and 5) sheets (Tormo et al., 1996).

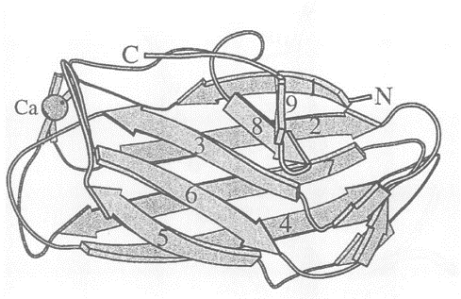

Figure 11. Ribbon diagram of the CBM3 from C. thermocellum CipA. Figure taken from (Tormo et al., 1996).

On top of the CBM3 structure forms a shallow groove composed by charged aromatic rings and polar residues. On the opposite side of the structure there is a planar surface that has proven to play an important role in cellulose binding (Figure 12). The flat strip is composed by a linear array of aromatic and charged residues, anchored to polar residues on the bottom sheet (Tormo et al., 1996). It has been suggested that recognition and the strong binding to the cellulose surface is the result of an interaction between the linear strip of aromatic residues and the glucose rings found along one of the cellulose chains (Bayer et al., 1998). Furthermore, it has been suggested that the aromatic residues in the CBM3a bind to the pyranose rings exposed on the hydrophobic (110) crystalline face of cellulose via hydrophobic interactions (Lehtiö et al., 2003; Georgelis et al., 2012).

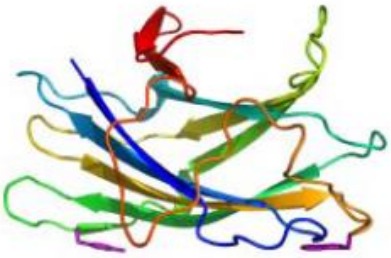

Figure 12. Three-dimensional structure of CBM3a The aromatic residues are colored purple. Figure taken from (Blake et al., 2006).

1.6.2. Applications of recombinant CBM

Thanks to their diversity and unique properties, CBMs have been fused with proteins, peptides, enzymes or other molecules, such as antibodies, via the recombinant DNA technology. The *Escherichia coli* bacterium has been used to produce recombinant CBMs. CMB-fusion technology can be used for different purposes: to facilitate the purification and production of small CBMs or specific peptides/proteins and to obtain recombinant proteins (Oliveira et al., 2015) (Figure 13).

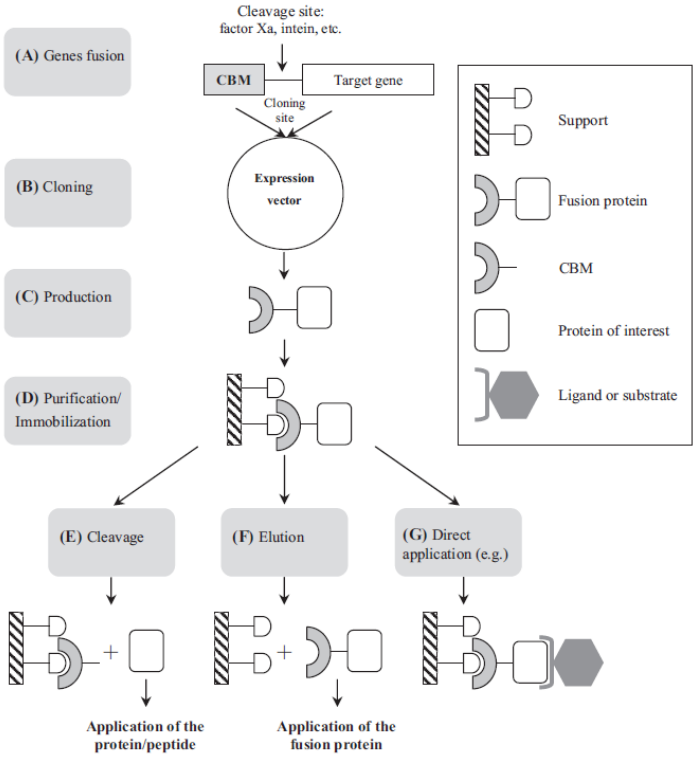

Figure 13. Recombinant CBM fusion technology A) fusion of genes coding for CBM and for the desired protein. The C-terminal or N-terminal of the target gene can be used to clone CBM, the fusion on N-terminal is represented here. B) Insertion of the gene into a plasmid vector. (C) Overexpression of the recombinant protein. (D) Purification of the recombinant protein by metal affinity chromatography using the attached his-tag (a tail of six histidines). (E) The protein is released from CBM link to support by proteolytic cleavage of the engineered sequence located between them. This aims to the application of CBM-free protein or peptide. (F) The recombinant protein is eluted from support, to be used for future applications. (G) The immobilized recombinant protein is directly promoting the link for a ligand or a substrate. Figure taken from (Oliveira et al., 2015) .

Recombinant CBMs have been used in different applications, some of which are described below. In the textile industry, the scouring process has been used in order to remove the cuticle layer of cotton fibers. This process is crucial to determine the quality of the product, because it affects the material's water absorption and dyeing efficiency (Oliveira et al., 2015). Degani et. al. monitored the efficiency of the cotton scouring process using a CBM recombined with the β-glucuronidase (CBM-GUS) reporter enzyme. During the process, the removal of the water-repelling components of the fiber cuticle increased the amount of available binding sites on the cellulose surface. In this case, the enhancement of the available cellulose fibers is proportional to the increase of CBM-GUS activity on a cotton fabric, making it possible to monitor the efficiency of the scouring process (Degani et al., 2004).

Recombinant fusions of CBM-bioactive peptides have also been used in the biomedical area. The use of this recombinant protein promotes not only a cell adhesion, but also a cell proliferation on the carbohydrate-based biomaterial (Oliveira et al., 2015). For example, Pértile et al. 2012 improved neuronal and mesenchymal cell adhesion by using the CBM3 fused with two different peptides - IKVAV and (IKVAV or (19) IKVAV) -, in order to modify the surface of the bacterial cellulose. (19) IKVAV comprises a sequence of 19 amino acids based on the proteolytic laminin fragment PA-22 that contains the IKVAV sequence. The adhesion of the neuronal and mesenchymal cells was improved when the (19)IKVAV-CBM3 was used, while the IKVAS-CBM3 showed a minimal effect on mesenchymal cell adhesion (Pértile et al., 2012).

Additionally, recombinant CBMs have been used in molecular diagnostic assays. Rosa et al. transformed a microfluidic paper-based analytical device (μPADs) into a bioactive device by recombining the fused CBM3 with a ZZ fragment. The ZZ fragment is derived from *Staphylococcus aureus* protein A, takes part in antibody binding. The bioactive paper with antibodies immobilized via CBM-ZZ has been tested for the detection of DNA from pathogenic micro-organisms, generating a signal on a specific zone of that paper detection device (Rosa et al., 2014).

2. The goal of this work

The main goal of this thesis is the development of silica-cellulose and titanium dioxide-cellulose composites by a biomineralization process. The synthesis of silica (SiO_2) and titanium dioxide (TiO_2) over cellulose fibers *in vitro* was mediated by the 19-mer synthetic peptide R5.

The first aim of the project was to promote precipitation of silica and titanium dioxide by using R5 at room temperature. Precipitation of silica and titanium dioxide was performed in phosphate buffer at pH 7 using TMOS and Ti-BALDH as precursor. In order to determine the amount of titanium dioxide and silica formed, two different methods were used. Firstly, the precipitates yields were determined by weighing dry matter. Next, the β-silicomolybdic and Tiron spectrophotometric assays were used to quantitate the amounts of silicon and titanium in the precipitates, respectively. The resulting nanoparticles were further characterized by scanning electron microscopy and dynamic light scattering.

The second and main purpose of the project was to produce composite materials of silica/cellulose and titanium dioxide/cellulose. Firstly, a fusion of R5 with CBM3 from *C. thermocellum* CipA was used to immobilize the templating peptide on a cellulosic matrix. Next, the matrix was incubated at ambient temperature with either a solution of TMOS or a solution of Ti-BALDH in phosphate buffer pH 7. The composites obtained by the CBM3-R5 fusion protein and the R5 peptide were compared. For this purpose, three different amounts (3 000 pmol, 30 pmol and 3 pmol) of recombinant CBM-R5 and R5 peptide were used in order to evaluate the density and distribution of the precipitated material on the cellulose surface. The morphology of the composite material was then analyzed by scanning electronic microscopy.

3. Materials and methods

3.1. Materials

3.1.1. Reagents

Ammonium molybdate tetrahydrate, oxalic acid dehydrate, metol, 4,5-dihydroxy-1,3-benzenedisulfonic acid disodium salt monohydrate (Tiron), titanium(IV) bis(ammonium lactate) dihydroxide (50 wt % in water) (Ti-BALDH) and tetramethyl orthosilicate (≥99%) (TMOS) were purchased from Sigma-Aldrich. Sodium sulphite anhydrous was purchased from Acros Organics. Sulphuric acid (<95%), HCl (~37%), acetic acid glacial were purchased from Fischer Chemical. Sodium acetate 3.hydratate, sodium phosphate monobasic, sodium phosphate dibasic were purchased from Panreac.

The 19-mer R5 peptide (SSKKSGSYSGSKGSKRRIL, 2013.30 g/mol) was synthesized by GeneCust and its purification was confirmed via HPLC-MS as ≥95%.

3.1.2. Recombinant Protein CBM3-R5

The gene CBM3-R5 was synthesized and inserted into a pHTP1 expression vector by Nzytech-Genes & Enzymes. A histidine tag was included at the N terminal for purification purposes. The final vector has 5973 bp with kanamycin resistance. The amino acid sequence of the CBM3-R5 fusion is shown in the following Figure 14.

MGSSHHHHHHSSGPQQGLRPVSGNLKVEFYNSNPSDTTNSINPQFKVTNTGSSAIDLSKL
TLRYYYTVDGQKDQTFWCDHAAIIGSNGSYNGITSNVKGTFVKMSSSTNNADTYLEISFTG
GTLEPGAHVQIQGRFAKNDWSNYTQSNDYSFKSASQFVEWDQVTAYLNGVLVWGKEPG
GSSKKSGSYSGSKGSKRRIL

Figure 14. Amino acid sequence of CBM3-R5 with199 residues. CBM3, R5 and his tag.

3.2. Methods

3.2.1. Synthesis of recombinant protein CBM3-R5

The plasmid pHTP1 containing the CBM3-R5 fusion gene was used to transform *Escherichia coli* BL21(DE3) competent cells (*E. coli* BL21 (DE3)) as following described.

a) Preparation of chemically competent cells

Preparation of inocula of *E. coli* BL21 (DE3) cells in LB (Luria-Bertani) medium was performed by adding 10 µl of a cryopreserved aliquot of cells to 15 mL conical centrifuge tubes with 5 mL of liquid LB medium. The culture was grown overnight at 37 ºC in an orbital incubator-shaker at 250 rpm. After reading the optical density measured at a wavelength of 600 nm ($OD_{600\ nm}$) on a Hitachi U-2001 UV/Vis Spectrometer, the inoculum was use to start cell growth with an initial optical density at 600 nm (OD_{600}) of 0.1 in a 100 mL Erlenmeyer containing 20 mL of LB medium. The culture was incubated at 37ºC in an orbital incubator-shaker until an OD_{600} of 1 is reached. Next, the cells were pelleted by centrifugation at 1 000 x g for 10 min at 4ºC. At the end, the supernatant was discarded and the pellet was re-suspended in 2 mL of the sterile cold TSS buffer [50 mM $MgCl_2$; 10% (w/v) PEG8000; 20 g/L LB; 5% (v/v) DMSO, at a final pH of 6.5]. Subsequently, the re-suspended cells were incubated on ice for 10 min. Aliquots of 100 µL of the competent cells obtained were then made and stored at -80 ºC.

b) Transformation of competent cells by heat-shock

The transformation was performed on ice by mixing 50 µl of chemically competent cells with 1 µl of 10 ng/mL of DNA plasmid pHTP1. The cells were left on ice incubation for 20 minutes. Then, heat shock was performed by heating the mixture for 1 minute at 42 ºC in a water bath and immediately the mixture was incubated on ice for 2 minutes. Then, the cells were resuspended in 950 µl of sterile LB medium and incubated at 37 ºC for 2 hours 30 minutes. Subsequently, the mixture was spin down for 1 minutes in a mini-centrifuge and at the end the cells were resuspended with supernatant. The cells were spread onto a plate in LB-agar supplemented with 30 µg/mL of kanamycin antibiotic and were incubated overnight at 37°C.

The transformants were selected by choosing the well-isolated colonies. Taking this into account, three colonies were picked from LB plates and grown in a 15 mL conical centrifuge tube with 5 mL of sterile LB medium, supplemented with 30 µg/mL kanamycin and were incubated overnight at 37 ºC with shaking (250 rpm). Then, the inoculum was used to start cell growth with an initial OD_{600} of 0.1 in a 15 mL conical centrifuge tube containing 5 mL of LB medium. This culture was incubated at 37 ºC in an orbital incubator-shaker until an OD_{600} of 1 was reached. Aliquots of cells were prepared with a final volume of 100 µL containing 17.5% glycerol and stored at -80ºC.

c) Bacterial cell growth for CBM3-R5 production

Preparation of a pre-inoculum of *E.coli* BL21 (DE3) cells transformed with pHTP1 was performed by adding 10 µL of a cryopreserved aliquot of cells to 15 mL conical centrifuge tube supplemented with 30 µg/mL kanamycin. The culture was putted to grow overnight at 37º and shacking at 250 rpm in an orbital incubator-shaker. Then, the pre-inoculum was used to prepared the inoculum with an initial OD_{600} of 0.2 in eight of 15 mL conical centrifuges each with 5 mL of LB medium with 30 µg/mL kanamycin and incubated overnight at 37 ºC with shaking (250 rpm) in an orbital incubator-shaker. After reading the OD_{600}, the cell suspension was pelleted by centrifugation 6 000 g for 3 minutes. In order to start a cell growth with an initial OD_{600} of 0.1 in 250 mL, cells were re-suspended and inoculated in two 500 mL

Erlenmeyer containing each 250 mL of LB medium supplemented with 30 µg/mL kanamycin and incubated at 37 ºC in an orbital shaker at 250 rpm.

When the growth reached an $OD_{600\ nm}$ of 0.5, the medium was supplemented with isopropyl β- D-1-thiogalactopyranoside (IPTG) to a final IPTG concentration of 1 mM in order to induce the synthesized of CBM3-R5. After 12 hours of induction, the cells were centrifuged at 4 000 g (Sorvall® RC-6 Plus superspeed centrifuge with SS34 rotor), 4ºC, for 10 minutes and the pellet was kept at -20 ºC until be used.

3.2.2. Purification of recombinant protein CBM3-R5

The cell was re-suspended in a minimum volume of 50 mM sodium phosphate buffer at pH 7 and disrupted by sonication pulse mode (BANDELIN ultrasonic homogenizer SONOPULS HD 3200, type MS 72) with 30 W at 6 minutes, cycles of 30 seconds in ice. Cell debris were removed by centrifugation at 9 000 g for 20 minutes at 4ºC and the resulting supernatant containing the fusion protein was filtered using a 0.22 µm syringe filter prior to chromatography. The purification of the CBM-R5 protein was performed by Ni-affinity chromatography using a HisTrap FF column of 1mL from in a Äkta 10 Purifier system (GE Healthcare). The column was equilibrated with 5 column volumes of buffer (10 mM imidazole, 50 mM NaHEPES, 1 M NaCl, 5 mM $CaCl_2$) and loaded with 2 mL of filtered supernatant. The column was washed with 20 column volume of the equilibration buffer and after with 20 column volumes of a similar buffer containing 35 mM imidazole. The CBM3-R5 protein was eluted with 20 column volumes of a buffer containing 300 mM imidazole and stored at -20ºC (Appendix).

The CBM3-R5 purity was evaluated by sodium dodecyl sulfate polyacrylamide gel electrophoresis (SDS-PAGE). The electrophoresis run was performed on polyacrylamide gels (resolving gel is composed by 12 % of total concentration of acrylamide (%T) and 3.3 % of concentration of the crosslinker (%C) and stacking gel are composed by 4% T and 3.3 %C). Samples (32.5 µl) were mixed with 12.5 µL loading buffer (4x) plus 5 µL of 1 M dithiothreitol and then they were denatured at 100 ºC for 10 minutes. A 10-250 kDa protein ladder from Bio-Rad was used as a molecular weight marker. The electrophoresis was performed at 90 V. The gels were stained with Coomassie Brilliant Blue and de-stained with a 10% acid acetic/30% ethanol solution. Images of the gels were obtained with a GS-800™ Calibrated Densitometer (Bio-Rad). The concentration of purified CBM3-R5 was determined by using the Pierce™ BCA (Bicinchoninic Acid) Protein Assay Kit according to the protocol from Thermo scientific – Microplate procedure (Thermo Fischer scientific Inc., 2002). For calibration curve, serum albumin was used as standard reference. Briefly, 25 µL of sample/standard was mixed with 200 µL of working reagent and then incubated at 37ºC for 30 minutes. The absorbances were measured at 562 nm. The diluent was composed by 8.3 mM NaHEPES, pH 7.5, 50 mM imidazole, 167 mM NaCl and 0.8 mM $CaCl_2$ was used as diluent. The purified CBM3-R5 was stored at -20º C until required (Appendix).

3.2.3. CBM3-R5 protein concentration and exchange buffer

Samples of purified CBM3-R5 were concentrated up to ~3 mM and exchanged against 50 mM phosphate buffer pH 7 using Pierce™ Protein Concentrators equipped with 10K MWCO polyether sulfone membranes according to the manufacturer's instructions (Thermo Fischer scientific Inc., 2014). Final concentration was determined by using the Pierce™ BCA Protein Assay Kit, according to the protocol from Thermo scientific – Microplate procedure (Thermo Fischer scientific Inc., 2002).

3.2.4. Silica precipitation assay

The *in vitro* silica precipitation was based on the method described by Kröger et al. (Kröger et al., 1999). A 1 M silicic acid solution was freshly prepared by dissolving TMOS in 1 mM aqueous HCl during 4 minutes before each assay. R5 was dissolved in 50 mM sodium phosphate buffer at pH 7 to a final concentration of 1.65 mM and final volume of 10 µL in a PCR tube. Then, 1 µL of silicic acid solution was added and the mixture was incubated at room temperature for 5 minutes. The reaction stopped by placing the tubes on ice and silica precipitates were separated by centrifugation at 14 000 g on a Hermle Z233 M-2 High Speed Microcentrifuge for 5 minutes. The supernatant was removed by pipetting and the silica-containing pellet was washed twice with milli-Q water and centrifuged as before. The pellet obtained was finally dried under vacuum overnight.

3.2.5. Titanium dioxide precipitation assay

In vitro precipitation of titanium dioxide was performed as described for silica. The R5 peptide was dissolved in 50 mM sodium phosphate buffer at pH 7 to a final concentration of 1.65 mM and final volume of 10 µL in a PCR tube. Then, 1 µL of 1 M aqueous solution of Ti-BALDH was added and the mixture was incubated at room temperature for 5 minutes. The reaction was stopped by placing the tubes on ice and titanium dioxide precipitates were separated by centrifugation at 14 000 g on a Hermle Z233 M-2 High Speed Microcentrifuge for 5 minutes. The supernatant was removed by pipetting and the titanium dioxide-containing pellet was washed twice with water milli-Q and centrifuged as before. The pellet obtained was finally dried under vacuum overnight.

3.2.6. Determination precipitate yield

In order to determine the yield of precipitated titanium dioxide and silica, the eppendorf PCR tubes were pre-weighed before precipitation (sections 3.2.4 and 3.2.5). After drying, the eppendorf tubes with silica and titanium dioxide pellets were weighed and the mass of each precipitate was determined by mass balance.

3.2.7. Silica quantification by β-silicomolybdate spectrophotometric method

The silicomolybdate test was used for quantification of silicon. Silicomolybdic acid (a yellow compound) is obtained through the reaction between monosilicic acid ($SiOH_4$, called as "soluble silica") and acidified ammonium heptamolybdate. The resulting compound can be measured spectrophotometrically at 400 nm (Coradin et al., 2004). However, the yellow silicomolybdic method has relatively high limit detection (10^{-4} mol/L) and suffers from interference from phosphate ions, which can exist in buffers or natural samples. The limit of detection can be improved to $5x10^{-6}$ mol/L by reducing silicomolybdic acid (e.g. with ascorbic acid, 1-amino-2-naphtol-4-sulphonic acid and 4-methylaminophenol sulphate (metol) to a molybdenum blue complex, which can be monitored at 810 nm, whereas the problem of phosphate ions can be solved by the addition of oxalic acid (Coradin et al., 2004).

3.2.7.1. The blue silicomolybdic assay

The silicomolybdate test was based on the protocol developed by Nelson and Arrington (Nelson and Arrington, 2010). An 8 g/L solution of acidified ammonium molybdate was prepared by dissolving 0.2 g of ammonium molybdate tetrahydrate in 10 mL of milli-Q water in a 25 mL volumetric flask, adding 1.2 mL of HCl 37 % and completing the volume to 25 mL with water. A metol-sulfite solution was prepared by dissolving 0.3 g of anhydrous sodium sulfite in 15 mL and then adding 0.5 g of metol (p-methylaminophenol sulfate). This solution was filtered (0.4 µm filter paper), transferred to a 25 mL volumetric flask and the final volume was completed with water. Solutions of 50 % (v/v) of sulfuric acid and 10 % (w/v) oxalic acid were also prepared.

A standard solution of 1 mM of silicic acid was obtained by preparing 1 M of TMOS in 1 mM HCl in order to facilitate the hydrolysis (4 minutes) and then 5 µL of this solution were transferred to a 5 mL volumetric flask and diluted to a final volume of 5 mL with water. Seven working standards were made by diluting the standard, 1 mM solution with water to 70 µM, 60 µM, 50 µM, 40 µM, 30 µM, 20 µM and 10 µM. A control sample was prepared by diluting 1 M TMOS to 91 mM, which was the initial concentration of silicic acid used in the precipitation reactions. In order to use this solution to check the performance of the assay, a 1:2000 dilution was performed to yield a final concentration of 45.5 µM silicic acid.

The collected dried pellets obtained from precipitation reactions were mixed with 10 µl of 1 M of sodium hydroxide at 95 ºC during 30 minutes performed by using Labnet AccuBlock™ Digital Dry Bath (block chamber D1102) in order to solubilize silica back. Sample preparation was completed by adding 20 µL of milli-Q water and then performing a 1:2000 dilution prior to the silicomolybdic assay.

The blue silicomolybdic assay was adapted to 96 well polystyrene microplates (Greiner Bio-one). Each well was loaded with 65 µL of the acidified ammonium molybdate solution (8 g/L) and with 162 µL of sample/working standards (triplicates). After 10 minutes, a freshly prepared solution of metol-sulfite

reagent, 10% oxalic acid, 50% acid sulfuric, water milli-Q (3:1:1:3.8) was prepared and 98 µL were added to each well. The blue color was left to develop over 2 hours at room temperature, before measuring the absorbance at a wavelength of 810 nm in a spectrophotometer SpectraMax Plus 384 Microplate. All measurements were repeated at least in triplicate.The absorbance was discounted with the absorbance of a blank (i.e. water).

Figure 15 shows the calibration curve obtained to determine the amount of silicon. The data is adequately described by the linear equation $\Delta Abs_{Si(OH)_4} = 0.0109\ [Si(OH)_4] + 0.0283$ (correlation coefficient of 0.9958).

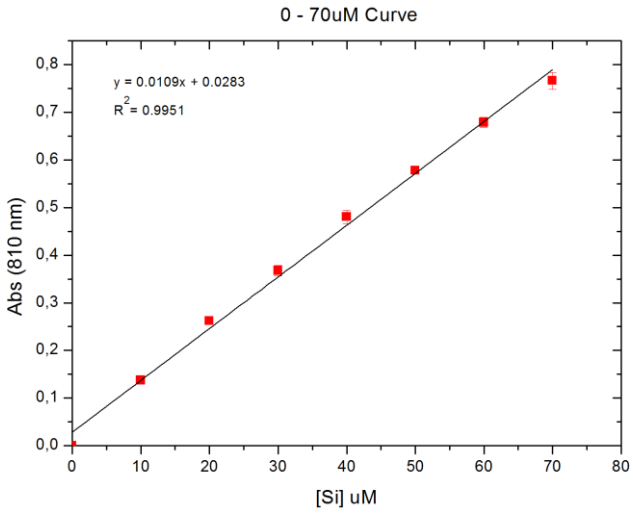

Figure 15. Determination of silicic acid by the silicomolybdic acid spectrophotometric method (blue assay).

3.2.8. Titanium supernatant quantification by spectrophotometric assay with tiron

Titanium was determined using Tiron (4,5-dihydroxy-1,3-benzene disulfonic acid), a reagent that reacts with titanium to form a soluble yellow Ti-Tiron complex which can be measured at 380 nm (Moharir, A.V., Sarma, K.A., Murti Krishna, 1972; Cole et al., 2006).

The assay was based on the method described by Cole et.al (Cole et al., 2006) and adapted to microplate with 96 polystyrene wells (Greiner Bio-one). A standard solution of 1 mM Ti-BALDH in 1.5 M sodium acetate buffer (pH 5.3) was used to prepare 7 working standards of titanium by dilutions with 1.5 M sodium acetate to 400 µM, 300 µM, 200 µM, 100 µM, 50 µM, 30 µM, 15 µM and 0 µM, respectively. A control sample with 91 mM of Ti-BALDH (initial concentration of titanium precursor used in the precipitation reactions) was prepared and diluted 1:1200 in order to yield a 76 µM solution. Each supernatant (8 replicas) was diluted 1:1200 like the control.

The Tiron spectrophotometric assay was performed in a 96 well polystyrene microplate (Greiner Bio-one). Each well was loaded with 20 µL of the 4% Tiron solution and with 180 ul of sample/working

standards (triplicates). The yellow color was left to develop over 1 hour at room temperature, before measuring the absorbance at a wavelength of 380 nm in a spectrophotometer SpectraMax Plus 384 Microplate. All measurements were repeated at least in triplicate. The absorbance was discounted with the absorbance of a blank

Figure 16 shows the calibration curve obtained to determine the amount of titanium. The data is adequately described by the linear equation ΔAbs = 0.0016 [Ti] +0.005 (correlation coefficient of 0.998).

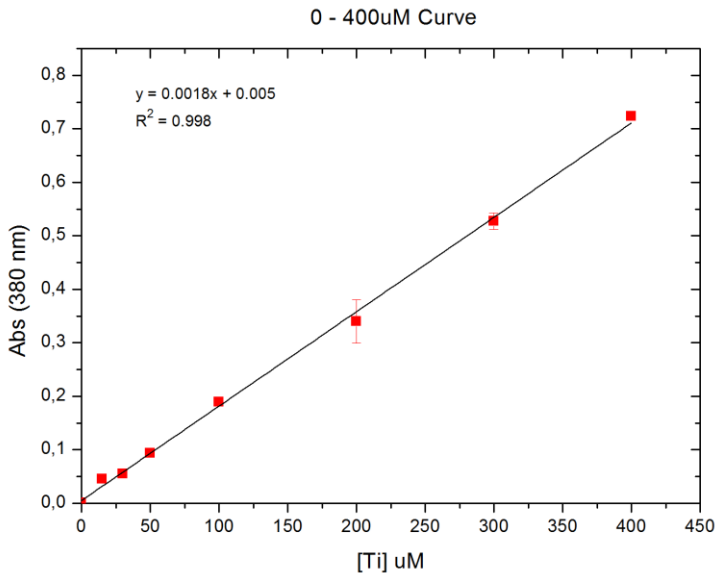

Figure 16. Determination of titanium by the Tiron complexation assay spectrophotometric method.

3.2.9. Scanning Electron Microscopy

Scanning electron microscopy (SEM) was used to analyze the morphology and evaluate the size of the particles silica and titanium dioxide synthesized as described in section 3.2.4 and 3.2.5, respectively. The precipitated material was washed, collected and then suspended in milli-Q water. A drop was added to a SEM support and left to dry. The sample was then coated with gold-palladium and analyzed with a scanning electron microscopy JSM – 7001F from JEOL. The SEM micrographs obtained were analyzed by a public domain image processing software ImageJ (National Institutes of Health) in order to measure the diameter of the particles.

3.2.10. Dynamic light scattering

Dynamic light scattering (DLS) measurements were conducted on Zeta Sizer Nano ZS from Malvern Instruments with a 633 nm laser (red laser) in order to evaluate the size of the nanoparticles. The Zetasizer system measures the Brownian motion and infers the diffusion coefficient of particles in

a suspension through the use of dynamic light scattering (Malvern instruments, 2004). The particle size, usually referred to as the hydrodynamic diameter, is then taken to be equivalent to the diameter of a sphere that diffuses at the same speed as the particles being measured. The results are typically displayed as number of particles in the population as a function of size (Nobbmann and Morfesis, 2009).

Glass cuvette were used in all measurements (10mm path length, 3.5 mL, spectrometer cell) at temperature of 25ºC and the scattering angle used was of 173º. Three measurements were performed for each sample and each one with 11 runs. The samples prepared as described above (sections 3.2.4 and 3.2.5) were resuspended in 1000 µL of milli-Q water after centrifugation at 14 000 g for 5 minutes. The measurements of the samples were performed before and after the sonication treatment pulse mode in BANDELIN ultrasonic homogenizer SONOPULS HD 3200 (type MS 72, 30W, for 3 minutes of sonication with cycles of 30 seconds) in order to reduce the obtained aggregates with precipitation reaction.

3.2.11. Silica/Titanium dioxide precipitation on paper via CBM-R5 and R5.

3.2.11.1. Chromatograhpy paper

Whatman no. 1 chromatography paper (catalog number: 3001-878) was used in all the assays. This paper is hydrophilic, homogeneous, pure, reproducible, biocompatible, available and inexpensive (Carrilho et al., 2009). The wax printing method (Xerox ColorQube 8570 color printer) was used to pattern arrays of 4 mm diameter circumferences (refereed as spot). The ink used is composed of a mixture of hydrophobic carbamates, hydrocarbons, and dyes that melts around 120 °C (Carrilho et al., 2009). After the printing, the paper was heated to 150 ºC on a heat plate for 2 minutes in order to melt the wax and allow it to diffuse vertically across the paper section. Thus, circular reaction areas confined by a uniform hydrophobic barrier were created that are able to contain aqueous liquids within.

3.2.11.2. Silica and titanium dioxide precipitation on the paper

Silica and titanium dioxide precipitation was performed in the same way. The concentration of the TMOS and Ti-BALDH precursors (91 mM) as also the reaction time (5 minutes) was the same used in the solution reaction precipitation. The composites obtained by CBM3-R5 recombinant protein and R5 peptide were compared in order to evaluate the effect of the CBM3-R5 immobilization in the distribution of the precipitated material on the cellulose fibers.

Three different concentrations of recombinant CBM-R5 and R5 peptide were tested in order to evaluate the density and distribution of the precipitated material. Briefly, 1 µl of buffer containing 3 000 pmol, 30 pmol or 3 pmol of R5 or CBM3-R5 were added to each circular reaction area and allowed to dry for 30 minutes at room temperature. Each circular reaction area was then individualized by cutting

paper into 1 cm x 1 cm squares. Precipitation reactions were then performed in 2 mL micro centrifuge tubes by immersing each square piece of paper in 1 mL of a 91 mM precursor solution in phosphate buffer at pH 7 for 5 minutes at room temperature. Protein-free controls were prepared by immersing paper pieces in the precursor solution. After 5 minutes of incubation, samples were taken from the solutions and let to dry at room temperature.

In the case of the silica, the silicic acid solution 1 M was freshly prepared by dissolving TMOS in 1 mM aqueous HCl during 8 minutes before each assay and then was prepared 91 mM of silicic acid solution.

3.2.11.3. The evaluation of the R5 immobilization via CBM3 or via physical adsorption

The R5 and CBM-R5 fluorescence was evaluated by taking some photos sob UV light (254 nm). For this purpose, was pipetted 1 µl of buffer solution containing 3 000 pmol or CBM3-R5 to each circular reaction being then left to dry for 30 minutes. Each circular reaction area was then individualized by cutting the paper into 1 cm x 1 cm squares. Then, each square piece of paper was immersed in 1 mL of phosphate buffer at pH 7 for 5 minutes at room temperature. The protein-controls were prepared by using the same protocol but they were not immersed, whereas the protein-free controls were prepared by immersing paper pieces in the phosphate buffer.

The dried papers and the protein-controls were submitted UV light in a dark UV chamber and some photos were taken. The obtained photos were analyzed by the ImageJ software. The photo was converted to 8-bit grayscale type and the mean gray value was measured, which correspond to fluorescence intensity.

4. Results and discussion

4.1. Precipitation of silica induced by the R5 peptide

A first set of experiments was set up to check the impact of R5 on silica precipitation. The experimental conditions used are summarized on the Table 1.

Table 1. Experimental conditions used in the R5-induced precipitation of silica and titanium dioxide in 50 mM phosphate, pH 7. Eight independent precipitations experiments were performed for silica and titanium dioxide.

Precursor solution (TMOS or Ti-BALDH)	
volume (µL)	1
concentration (mM)	1000
mass (nmol)	1000
R5 solution	
volume (µL)	10
concentration (mM)	1.65
mass (nmol)	16.5
Precipitation mixture	
volume	11
precursor concentration (mM)	91
R5 concentration (mM)	1.5
Precipitation time (min)	
5	

In these experiments, silicic acid solutions in phosphate buffer at pH 7 were added either to phosphate buffer (Figure 17, right) or to phosphate buffer with 1.5 mM R5 (Figure 17, left). While no precipitation was observed in the absence of the peptide (Figure 17, right), a white turbidity rapidly developed in about 30 seconds when the silicic acid was contacted with the peptide solution (Figure 17, left). This result confirmed that R5 is required to promote silica precipitation.

Figure 17. Silica precipitation with 1.5 mM R5 and 91 mM silicic acid at pH 7 (left). A control was performed without the addition of R5 7 (right).

The dry weight of silica precipitated in the presence of R5 was determined next on the basis of eight replicas of the experiment. Previous results have shown that the dry weight of R5-induced silica precipitates is linear with silicic acid concentration (Senior et al., 2015). For example, Senior et al. obtained about 13 mg ml^{-1} of silica precipitate mediated by 1.5 mM of R5 peptide with 50 mM of the initial concentration of silicic acid (Senior et al., 2015). Here, the dry weight of silica precipitate obtained with 91 mM of silicic acid was 0.2±0.04 mg, which results in a concentration of 21.4 ± 3.4 mg ml^{-1} (Table 2). Taking into account that the dry weight is linear with silicic acid concentration, it makes sense that the value (21.4 ± 3.4 mg ml^{-1}) obtained with 91 mM is greater than the value obtained with 50 mM.

Table 2. R5-induced precipitation of silica in 50 mM phosphate buffer, pH7. A precipitation time of 5 minutes was used. The results shown correspond to averages of eight independent precipitation experiments.

Mass (mg)	0.23 ± 0.04
Concentration (mg/ml)	21.4 ± 3.5
Silica (nmol)	713.1 ± 182.4
Specific activity (nmol/min.nmolR5)	8.6 ± 2.2

Furthermore, indirect quantification of the silicon on the precipitates was achieved by digesting silica pellets with NaOH and determining the dissolved silica (essentially monosilicic acid, $Si(OH)_4$ using the β-silicomolybdic acid spectrophotometric method (Kröger et al., 1999; Coradin et al., 2004). For the experimental conditions used in this work (11 µL, 91 mM silicic acid, 1.5 mM (16.5 nmol) R5, phosphate buffer pH 7), the amount of silicon precipitated after 5 minutes was 713.1 ± 182.4 nmol (Table 2). Kroger et al. obtained about 380 nmol of silica when using 2.55 mM of the R5 peptide and 91 mM of silicic acid at pH 7 (Kröger et al., 1999). Senior et al. reported that silicification appears to have a cooperative response for peptide concentration, where 1.5 mM of peptide showed precipitate lower than 2.5 mM (Senior et al., 2015). Thus, the amount of precipitated silicon obtained here with 1.5 mM peptide is higher. The specific silica precipitation activity obtained here was 8.6 ± 2.2 nmol Si/min.nmol R5, which is of the order of magnitude of the specific activity of 3.59 ± 0.16 nmol of Si/min.nmol R5 obtained with 2 mM of R5 by Knecht and Wright (Knecht and Wright, 2003).

4.2. Size measurements of SiNPs conducted by DLS

The size of the silica nanoparticles obtained as described in the previous section was evaluated using a Zetasizer system. The precipitated particles (~0.23 mg, see Table 2) were centrifuged and re-suspended in 1 mL of miliQ water. Triplicate measurements of this suspension were performed by DLS. The obtained results show a significant dispersion in the size distribution of the particles (Figure 18 a-c), with average sizes varying from 260 ± 12 nm to 699 ± 123 nm (Table 3, #1).

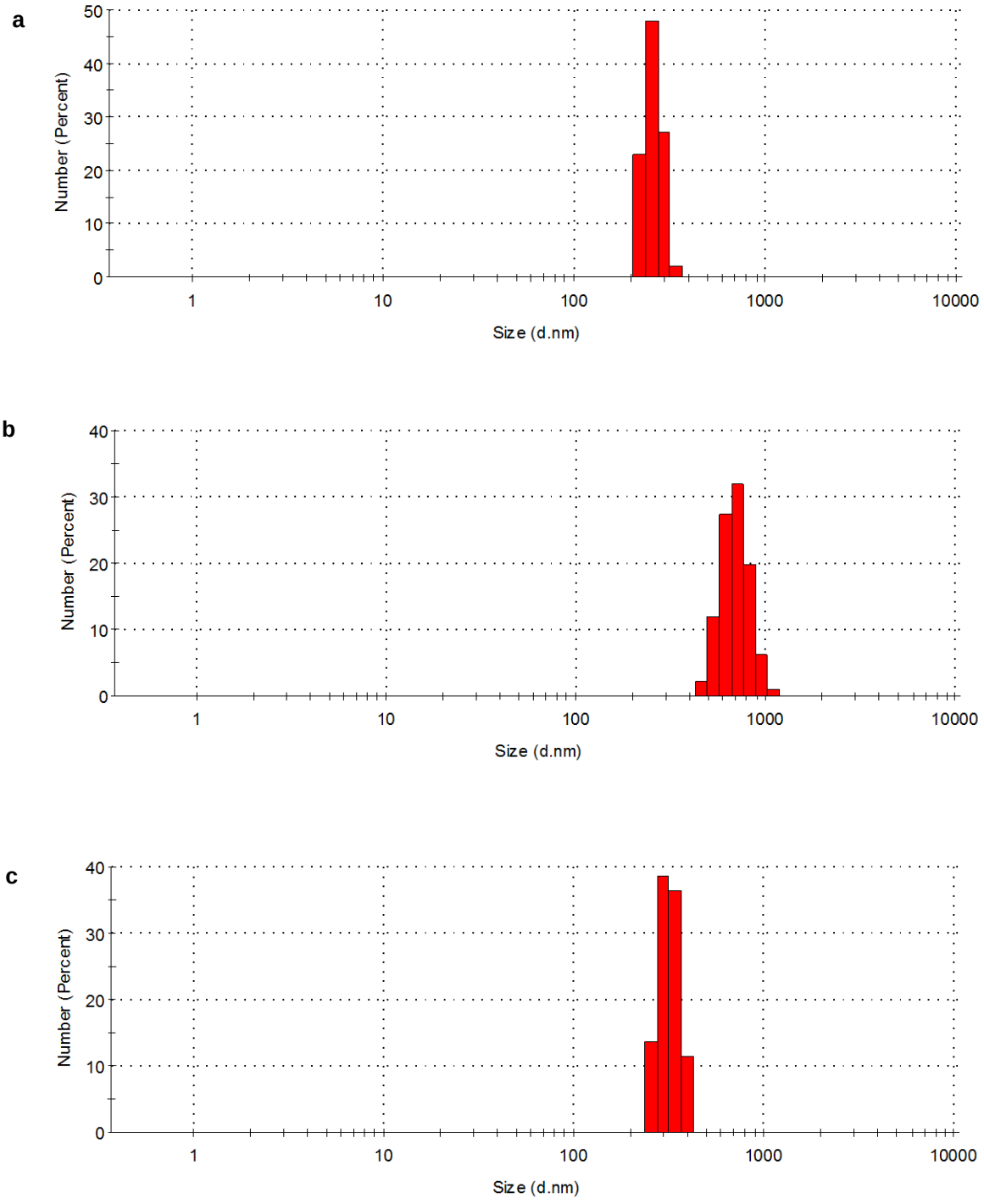

Figure 18. Size distribution of silica particles obtained by precipitation with R5. Determinations were made by analyzing ~ 0.23 mg of silica suspended in 1 ml of water by DLS. The histograms of the number-size distribution (a, b, c) correspond to three measurements made on the same sample.

Figure 18 shows that the three size measurements of the same sample were not consistent between them. This sample exhibits a mean polydispersity index value (PDI) of 0.85 ± 0.25 (table 3, #1). PDI values over 0.5 indicate that the samples have large size distributions, whereas monodisperse samples have a PDI value below 0.1 (Malvern instruments, 2004). The high PDI index obtained can be due to the aggregation that happens during the precipitation reaction, which promotes different size clusters and difficult the analysis of the size of a single nanoparticle.

In an attempt to reduce the dispersion of the result obtained and with the goal of reducing possible particle aggregates, the sample was subjected to ultrasonic treatment (#2) and diluted (1:4) and subjected to ultrasonic treatment (#3).

Table 3. Average size of silica particles prepared by precipitation with R5 as obtained by DLS. Three size measurements (a, b, c) were performed for a silica sample re-suspended (~0.23 mg) in 1 mL of milli-Q water and subjected to: #1 –no treatment, 2# - ultrasonic treatment for 3 minutes and 3# - 1:4 dilution and ultrasonic treatment for 3 minutes. The mode is shown for each measurement. In some cases, two populations were detected the corresponding number percentage for each sub-population is shown in brackets. The average of the mode obtained is also shown alongside with the mean PDI value.

SAMPLE	a (nm)	b (nm)	c (nm)	Average (nm)	PDI
#1	260 ± 29	699 ± 123	318 ± 41	426 ± 239	0.85 ± 0.25
#2	134 ± 27 (93.9%)	607 ± 184 (98%)	807 ± 312 (99.5%)	558 ± 332	0.52 ± 0.06
	1004± 312 (6.1 %)	3273 ± 1101 (2%)	4837 ± 868 (0.5%)		
#3	182 ± 25	226 ± 64 (24 %)	150 ± 97	152 ± 29	0.61 ± 0.15
		92 ± 17 (75.5%)			

However, the size measurements obtained were inconclusive (Table 3). The PDI of the sample decreased from the first treatment (#1) from 0.85 ± 0.25 to 0.52 ± 0.06 using ultrasonic treatment, which can mean that the size of the particles obtained in the first treatment (#1) was affected by the sonication action once the clusters broken up into smaller particles/clusters. Furthermore, the second treatment (#2) revealed the presence of a smaller (0.5% to 6.1% in % number of the particles) particle sub-populations.

In order to further decrease the aggregates, a dilution of 1:4 and an ultrasonic treatment were performed (Table 3, #3). In this sample treatment, the size of the particles decreased to a mean value of 151.92 nm, but the PDI increased to 0.61 ± 0.15. In spite of the ultrasonic and dilution treatment, the size distribution of the particle remained very broad, as judged by the high PDI values. Thus, these results indicate that the particles produced by R5 and TMOS have different sizes and are likely to be present as clusters.

4.3. Size and morphology of SiNPs analyze through SEM

SEM was used next to complement the DLS measurements and to observe the morphology of the particles of R5-precipitated silica (Figure 19).

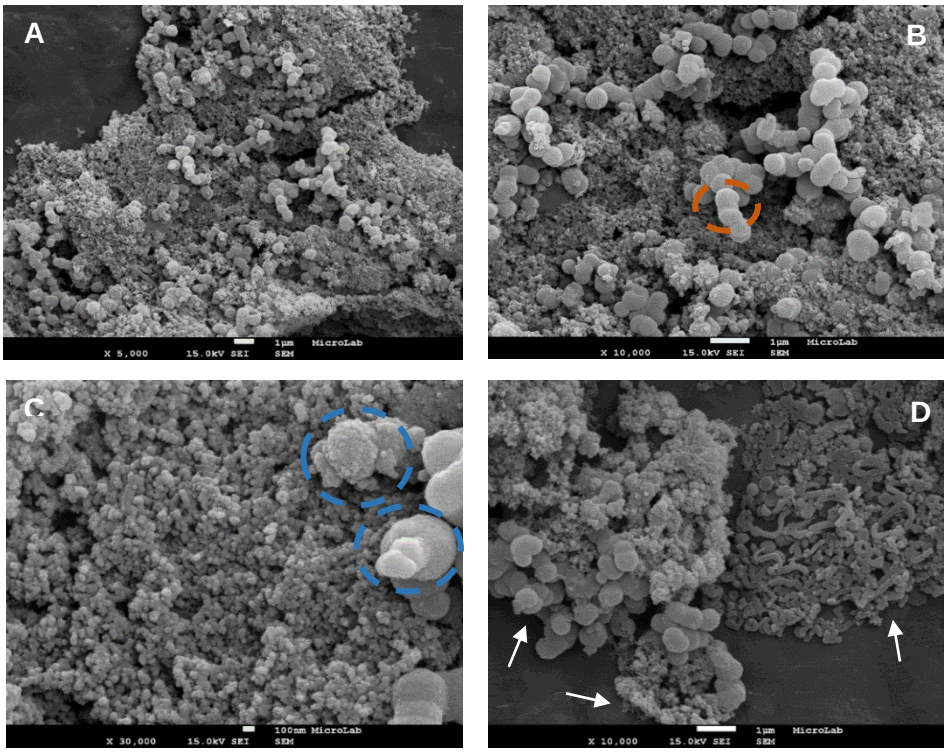

Figure 19. SEM micrographs of SiNPs induced by R5. The A, B and D have a scale bar of 1 µm and C has a scale bar of 100 nm. B and D have micrographs at magnification of x 10,000. A and C have magnifications of x 5,000 and x 30,000, respectively. Arrows indicate three different main populations of morphologies/size of SiNPs. The circles indicate what seems to be fused small particles into a large particle (blue circle) and fusion between two particles (orange circle).

The lower magnification micrograph in Figure 19A shows that the silica precipitated by R5 is characterized by a heterogeneous size distribution and by the presence of large clusters of SiNPs. In terms of size, two main populations of spherical SiNPs are clearly observed in Figures 19B and 19C. The population with larger size is characterized by particles with diameters around 538 ± 77 nm, whereas the population with smaller sizes, which seems to predominate, is characterized by diameters of the order of 37 ± 6 nm. Fusion between two or more spherical particles can also be observed, especially for the case of the larger particles (see fused particles circled in orange in Figure 19B). The smaller silica particles are highly connected between them, forming dense and fused aggregates (Figure 19C). Also, it appears that the smaller particles are fused together, creating larger particles (Figure 19C, blue circles). This size discrepancy does not seem to be characteristic of this peptide. According to previous reports, Nam et al obtained SiNPs with sizes in the range of 600 to 700 nm (Nam et al., 2009), Knecht

and Wright reported SiNPs with a range of 250 to 450 (Knecht and Wright, 2003), Senior et al and Naik et al obtained SiNPs with a size of about 500 nm (Naik et al., 2003; Senior et al., 2015).

In addition to the spherical morphology of SiNPS, clusters of elongated forms of silica with different lengths were also observed, some of which are rolled up on themselves (Figure 19D). This morphology was not expected because the R5 peptide have been reported to produce spherical morphology particles under static conditions (Naik et al., 2003).

These results justified the broad distribution of size and the inconsistency between the measurements obtained with DLS technique, once the silica material is composed by different sizes and particle morphologies and, among these, they are aggregates.

4.4. Precipitation of titanium dioxide induced by R5

As in the case of silica, R5 is also required to promote amorphous titanium dioxide precipitation from the precursor Ti-BALDH under ambient conditions. The conditions of the precipitation were the same for silica precipitation and are summarized in the Table 1. The peptide induced almost instantly the titanium dioxide precipitation, originating a large turbidity (Figure 20, right). No titanium dioxide precipitation was observed in the absence of the peptide at room temperature (Figure 20, left).

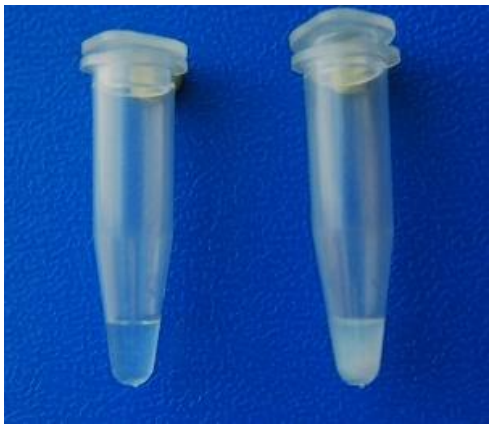

Figure 20. Titanium dioxide precipitation with 1.5 mM R5 and 91 mM titanium precursor at pH 7 (right). A control was performed without the addition of R5 7 (right).

The dry weight of the titanium dioxide precipitate obtained was 0.12 ± 0.04 mg, which results in a concentration of 11.0 ± 4.6 mg ml^{-1}. The titanium left in the supernatant after precipitation was halted was further quantified by the Tiron complexation assay and used to estimate the amount of precipitated titanium by mass balance (Table 4).

Table 4. R5-induced precipitation of titanium dioxide in 50 mM phosphate buffer, pH 7. A precipitation time of 5 min was used. The results shown here correspond to averages of eight independent precipitation experiments.

Mass (mg)	0.12 ± 0.04
Concentration (mg/ml)	11.0 ± 4.6
Titanium (nmol)	492.0 ± 85.0
Specific activity (nmol/min.nmolR5)	6.0 ± 1.0

The amount of precipitated titanium after 5 minutes was 492.0 ± 85.0 nmol with the same conditions used for silica precipitation (11 µL, 91 mM titanium, 1.5 mM (16.5 nmol) R5, phosphate buffer pH 7), (Table 4). Comparing this result with the previous one reported by the authors, in which they obtained at least 50% of incorporated titanium in the precipitate (Cole et al., 2006), the obtained result in this work is concordant (~49.1%). The specific activity of R5 for titanium precipitation was of 6.0 ± 1.0 nmol of Ti/min.nmol R5. This result is of the order the same magnitude obtained in previous reports, for example, Sewell and Wright obtained a specific activity of 2.16 ± 0.23 nmol Ti/min.nmol R5.

4.5. Size measurements of TiNPs conducted by DLS

The size of TiNPs induced by R5 as described in the above section was analyzed by Zetasizer system.

The previous centrifuged titanium dioxide material (~0.12 mg) was re-suspended in 1 mL of water milli-Q and three size measurements were performed by DLS (Figure 21 a,b,c, Table 5). The suspension revealed a broad dispersion in the range of 219 ± 37 nm to 3464 ± 390 nm.

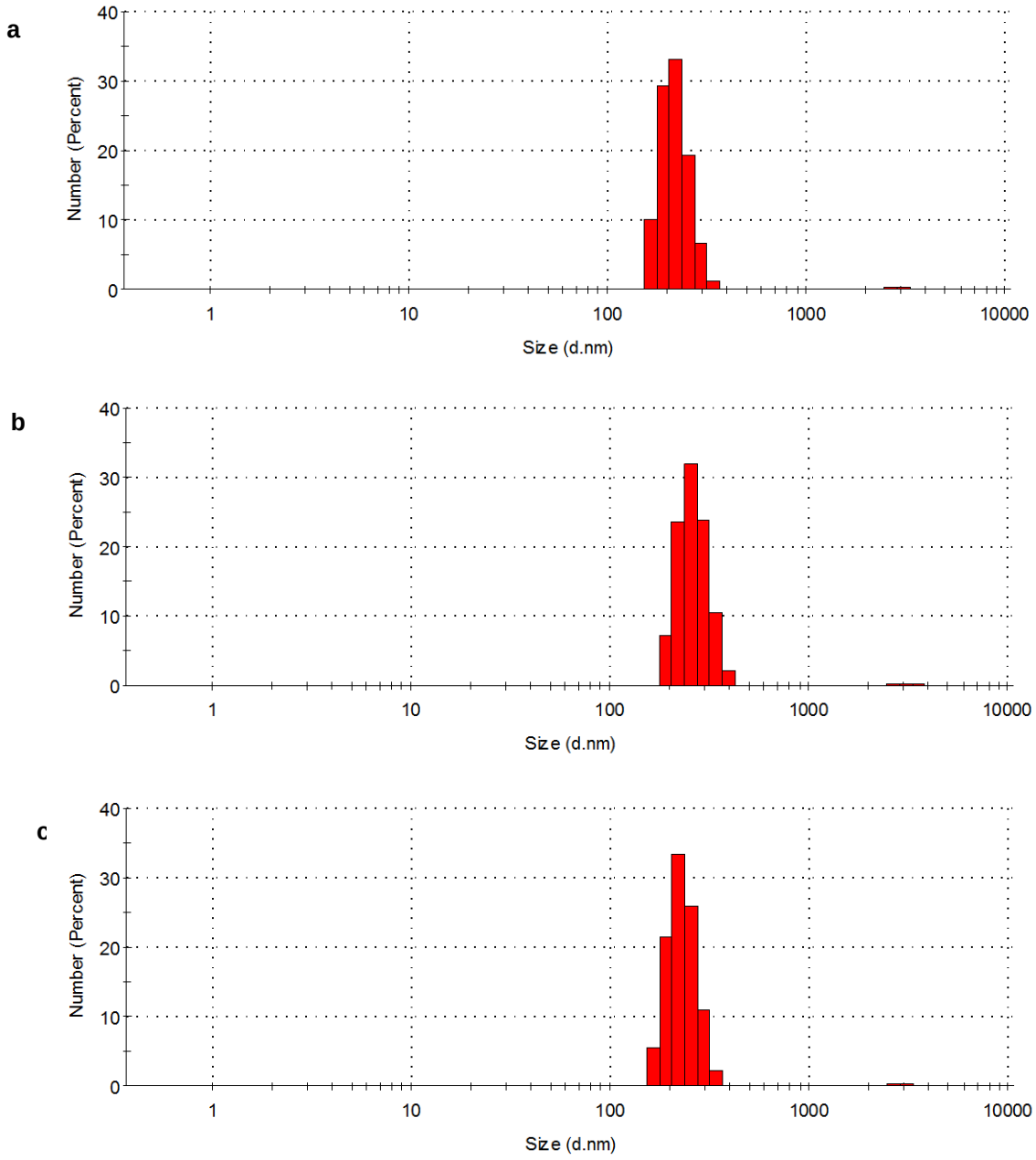

Figure 21. Size distribution of titania particles obtained by precipitation with R5. Determinations were made by analyzing ~ 0.12 mg of titania suspended in 1 ml of water by DLS. The histograms of the number-size distribution (a, b, c) correspond to three measurements made on the same sample.

The three size measurements obtained a PDI value of 0.77 ± 0.08, which means that the suspension has a high polydispersity of particle size (Table 5, #1). This high polydispersity can be due the presence of the aggregates of the particles, which affect the size measurement by DLS. However, we can observe that in three measurements, the main size distribution is in the range of 200 nm (Table 5, #1).

In order to decrease the large distribution as well as the PDI value, were made two treatments of the samples: an ultrasonic treatment for 3 minutes (30 W) (Table 5 #2) and another with a diluted sample (1:4) and an ultrasonic treatment (Table 5).

Table 5. Average size of titanium dioxide particles prepared by precipitation with R5 as obtained by DLS. Three size measurements (a, b, c) were performed for a titanium dioxide sample re-suspended (~0.12 mg) in 1 mL of milli-Q water and subjected to: #1 – no treatment, 2# - ultrasonic treatment for 3 minutes and 3# - 1:4 dilution and ultrasonic treatment for 3 minutes. The mode is shown for each measurement. In some cases, two populations were detected - the corresponding number percentage for each sub-population is shown in brackets. The average of the mode obtained is also shown alongside with the mean PDI value.

SAMPLE	a (nm)	b (nm)	c (nm)	Average (nm)	PDI
#1	219 ± 37 (99.4%)	264 ± 99 (99.3%)	230 ± 39 (99.3%)	258 ± 26	0.77 ± 0.08
	3067 ± 762 (0.6%)	3464 ± 390 (0.7%)	3143 ± 816 (0.7%)		
#2	134 ± 57 (0.7%)	80 ± 28	83.4 ± 28.7	69 ± 22	0.48 ± 0.01
	42.72 ± 8.35 (99.3 %)				
#3	618 ± 210 (0.1%)	573 ± 204 (0.1 %)	150 ± 97	106 ± 72	0.48 ± 0.02
	99 ± 22 (99.9%)	88 ± 20 (99.9%)			

The ultrasonic treatment appeared to affect the size measurement, once the size of particles/aggregates decreased from 257.74 ± 0.08 to 69.03 ± 22.28 nm of diameter and the PDI value decreased to 0.48 (Table 5, #2). Moreover, the population with a range of 1000 nm of diameter, which was detected by DLS in the first analysis (Table 5, #1), did not appear after the ultrasonic treatment (Table 5, #2), which can mean that these large aggregates were broken up into smaller aggregates or particles.

A final treatment (dilution and ultra-sonication) was made in order to evaluate if the size distribution continues to decrease (Table 5, #3). The obtained result of the size measurement (#3) was not consistent with the size measurement from second analysis (#2). It was expected that the PDI value decreased in order to have a size population with more homogenous distribution. However, the PDI value was maintained, 0.48 ± 0.02, and the size of the particles/aggregates increased (105.83 ± 72.32 nm). This result can be attributed to the existence of the fused particles as well as the presence of aggregates, which affected the DLS analysis.

4.6. Size and morphology of TiNPs analyze by SEM

In order to evaluate the morphology as well as the size of the particles induced by 1.5 mM R5 and 91 mM titanium precursor for 5 minutes, SEM analysis were made (Figure 22)

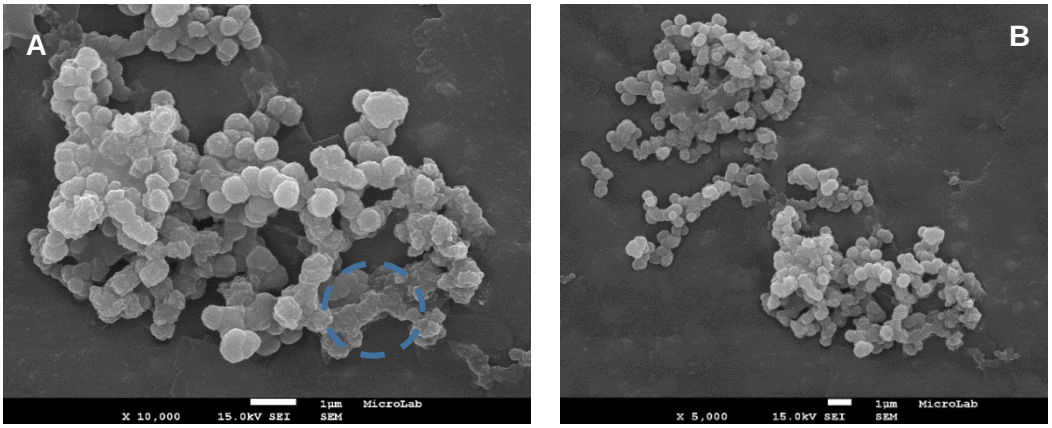

Figure 22. SEM micrographs of TiNPs induced by R5. Scale bar of 1 µm. A and B micrographs have magnifications of x 10, 000 and x 5, 000, respectively.

The SEM micrographs (Figure 22) of the spherical TiNPs showed a diameter of about 479 ± 91 nm (Figure 22). In the Figure 22 (A), is possible to observe TiNPs clusters, where the particles are fused between them. Moreover, the surface particles seem to be rough (Figure 22, B). There are structures that appeared to be a result of the consecutive fusion between the particles, which do not allow to distinguish spherical single particles (circle blue). These aggregates affect the measurement by DLS. According to the previous works, different sizes of titanium dioxide particles were obtained, such as 50 ± 20 nm (Sewell and Wright, 2006) and 3.2 ± 1.5 µm (Cole et al., 2006).

The SEM results, allows to explain the inconsistency of the DLS analysis, once the particles showed some fusion between the spherical ones and also there are some irregular titanium dioxide structures.

4.7. Precipitation of silica and titanium dioxide induced by CBM3-R5

A CBM3-R5 fusion was designed, produced and purified with the goal of immobilizing the R5 peptide in cellulose matrices and attempt to precipitate silica and titanium dioxide *in situ*. An initial set of experiments was performed to investigate the ability of the CBM3-R5 fusion to promote precipitation in solution. The results showed that the silica precipitation activity of R5 was not affected by its fusion with CBM3. The morphology of the precipitate obtained with 1.5 mM CBM3-R5 and 91 mM of TMOS at pH 7 in the 50 mM phosphate buffer was observed through SEM analysis and compared with the morphology of SiNPs obtained only with R5 (Figure 23).

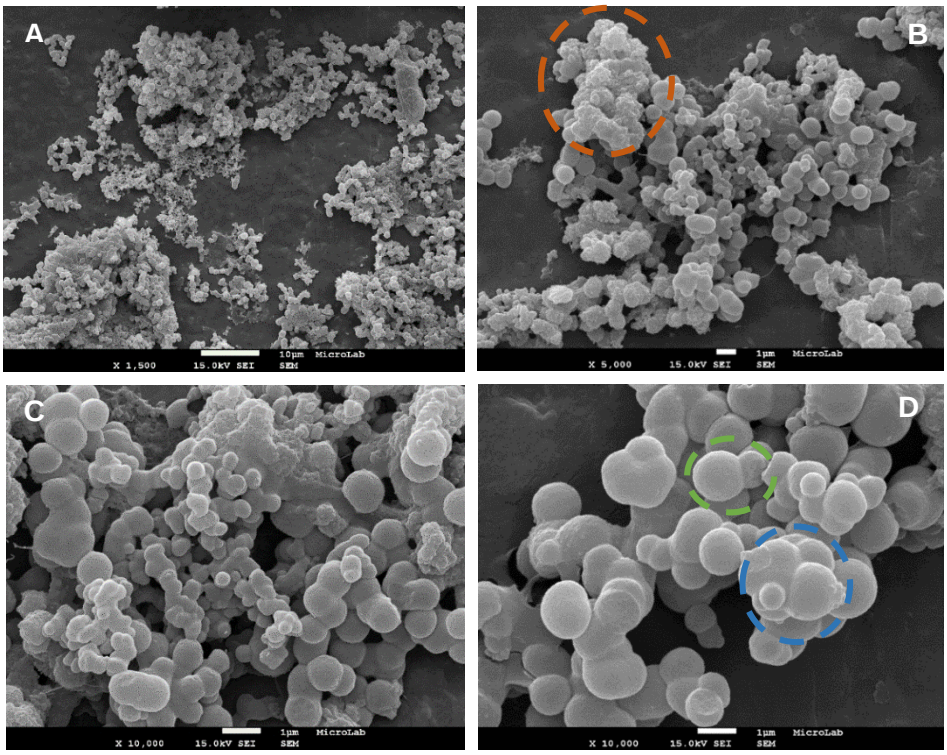

Figure 23. SEM micrographs of SiNPs induced by CBM3-R5 in 50 mM phosphate buffer at pH 7. Micrographs were obtained with magnifications of x 1, 500 (A), x 5, 000 (B) and x 10, 000 (C, D). Scale bar corresponds to 10 µm in A and to 1 µm in B-D.

As can be observed, the fusion protein induces the formation of partially homogenous spherical silica particles with sizes around 820 ± 179 nm, larger than the particles obtained with R5 (Figure 23). Immobilization of proteins by using DNA technology in order to fuse R5 with a protein of interest has been reported. The encapsulation method allows the self-immobilization *in vitro* of the recombinant protein during silica formation (Nam et al., 2009; Choi et al., 2011). In the SEM micrograph we can observe some clusters of the particles (Figure 23A). Moreover, is possible to see fused spherical particles (Figure 23D, green circle) and also the fusion between smaller particles that seems to form the bigger particles (Figure 23D, blue circle). Thus, like other samples, the spherical SiNPs are found fused and connected. Some structures with an irregular morphology were also detected, which seem to be a result of the connection and fusion of the silica particles (Figure 23B orange circle).

The CBM3-R5 protein was also able to induce titanium precipitation in solution (Figure 24). As with the silica particles, aggregated spherical particles of titanium dioxide with sizes around 528 ±77 nm and some fused particles were also observed.

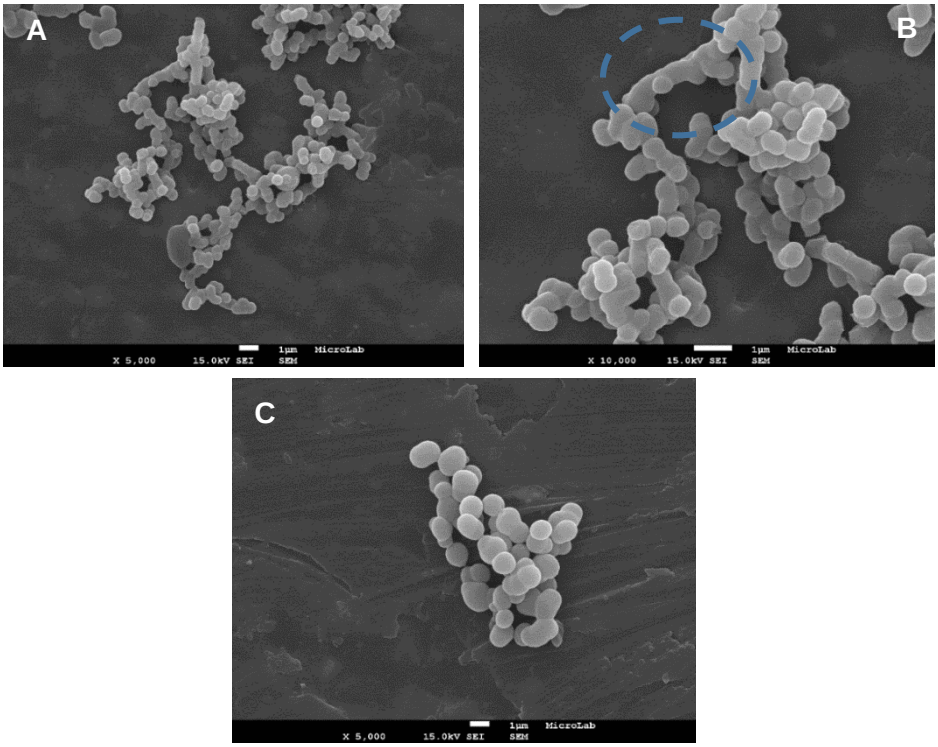

Figure 24. SEM micrograph of TiNPs induced by CBM3-R5 in 50 mM phosphate buffer at pH 7 (scale bar of 1 µm). Micrographs were obtained with magnifications of x 5, 000 (A, C) and x 10, 000 (B).

In similar with SiNPs obtained with this protein, it was observed clusters of the TiNPs, where the TiNPs are hardly connected to each other (Figure 24A). In addition to partially spherical morphology, elongated structures were observed, which seem to result from the fusion between the TiNPs (Figure 24C, blue circle). In Figure 24C, it is possible to see a cluster of the spherical TiNPs leading to a conclusion that they have tendency to be fused between them in order to form a bigger particle, as observed as well for SiNPs.

4.8. Precipitation of SiNPs on paper via CBM-R5 and R5

4.8.1. Immobilization of R5 on the paper via CBM3 or via physical adsorption

The ability of R5 and CBM3-R5 to precipitate SiNPs on chromatographic paper was evaluated. For this purpose, circular reaction areas (4 mm diameter) defined by a uniform hydrophobic barrier were first created on the paper that are able to contain aqueous liquids within. Next, certain amounts R5 or CBM3-R5 (1 µL, 3 000 pmol) were added to each circular reaction area and allowed to dry for 30 minutes at room temperature. Each circular reaction area was then individualized by cutting paper into 1 cm x 1 cm squares. Observation of the reaction areas under 254 nm UV light showed that the peptide emitted an intrinsic fluorescence, most likely due to the presence of tyrosine (Y), a residue that can be excited at wavelengths ranging from 250 nm to 310 nm (Hospes et al., 2013).

The fluorescence of the circular areas before and after the immersion of the paper squares in phosphate buffer for 5 minutes was analyzed and compared using the ImageJ software (Figure 25). When R5 alone was added, the fluorescence predominated mainly at the outskirts of the spot (see circular area 3 in Figure 25), whereas when CBM3-R5 was added, the fluorescence was more evenly distributed (see circular area 1 in Figure 25). This indicates that R5 diffuses outwards during evaporation as a result of a phenomenon akin to the “coffee ring” effect. In the case of CBM3-R5, binding of the fusion protein to the cellulose fibrils via affinity prevents this from happening.

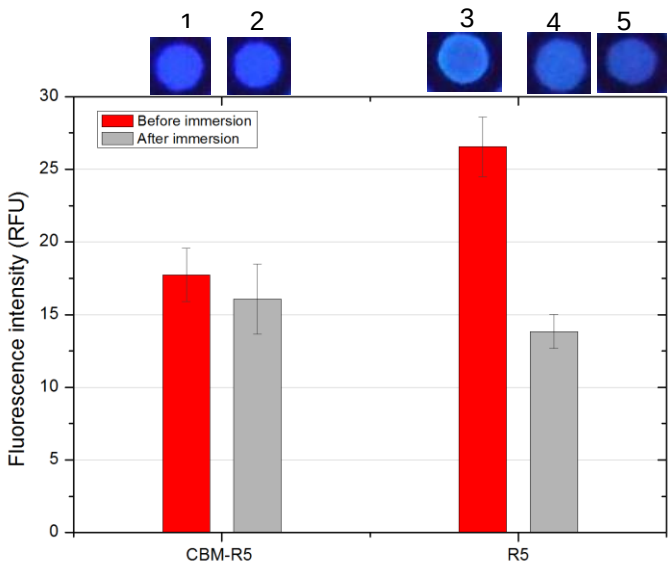

Figure 25 Fluorescence intensity obtained by R5 physically adsorption and R5 immobilized by CBM3. Red color corresponds to fluorescence intensity before the immersion on the phosphate buffer 50 mM, pH 7 and the grey color correspond to the fluorescence intensity after the immersion. Photos were taken under UV light (253 nm) 1- CBM3-R5 before the immersion, 2- CBM3-R5 after the immersion, 3- R5 before the immersion, 4- R5 after the immersion and 5- control with 50 mM phosphate buffer pH 7.

It is also possible to observe that there is a large decrease in fluorescence intensity after the immersion of the paper pieces with R5 on buffer, whereas in the case of CBM3-R5 the decrease was more modest (Figure 25). This suggests that physical adsorption is not enough to immobilize this peptide on the paper. Meanwhile, CBM3 fused with R5 appeared to be more efficient when immobilizing R5 on the paper than physical adsorption. The CBM3-R5, before and after the immersion, was shown to lose some residual fluorescence intensity. This can be attributed to the proteins that do not bind to the cellulose. It was not possible to analyze these results with 30 pmol and with 3 pmol due to the fluorescence intensity not being visible.

4.8.2. Silica precipitation on paper

A set of experiments were performed to evaluate if the immobilized CBM-R5 and R5 were able to drive silica precipitation on paper. Pieces of paper were prepared as described above with three different amounts of CBM-R5 and R5 (3 000 pmol, 30 pmol and 3 pmol). Precipitation reactions were then performed by immersing each square piece of paper in 1 mL of a 91 mM solution of silicic acid in phosphate buffer at pH 7 for 5 minutes at room temperature (Table 6). As control, paper pieces without protein were used, which were also immersed in silicic acid solution. After 5 minutes of incubation, samples were taken from the solutions and let to dry at room temperature.

The analysis of the results paper assays was a big challenge as the silica material is a white compound, which shares the same color as the paper. In fact, no differences in the aspect of the circular areas were observed by visual inspection. Thus, the analysis of precipitation on paper was highly dependent on SEM.

Clear differences in the results were observed when circular areas of paper prepared with 3 000 pmol of CBM3-R5 and R5 were observed at lower magnification by SEM.

As it is possible to observe in Figure 26, which shows a composite image of areas prepared with R5 (left) and CBM3-R5 (right), formation of SiNPs reveals itself by the presence of a whitish material that contrasts strongly with the paper background. Furthermore, it is very clear that CBM3-R5 allows silica precipitation to occur over the entire surface of the paper circle (Figure 25, right), whereas in the case of R5 silica precipitation occurred mostly at the inner periphery of the circular area (Figure 25, left). These results are in accordance with the analysis of protein distribution by fluorescence intensity presented in the previous section, and indicate that silica precipitation is co-localized with R5. Thus, a more uniform immobilization of R5 and hence of SiNPs was possible with the CBM3-R5 fusion because CBM3 contains binding sites involved in the recognition of the flat surface of crystalline cellulose (Tormo et al., 1996). Also, it seems that the R5 did not affect the ability of the CBM3 to bind to cellulose. When R5 was used alone, immobilization and silica precipitation on the cellulose surface were clearly more heterogeneous, with the peptide and silica predominating in the circle periphery. As expected, no silica particles were observed in the control experiments performed without protein.

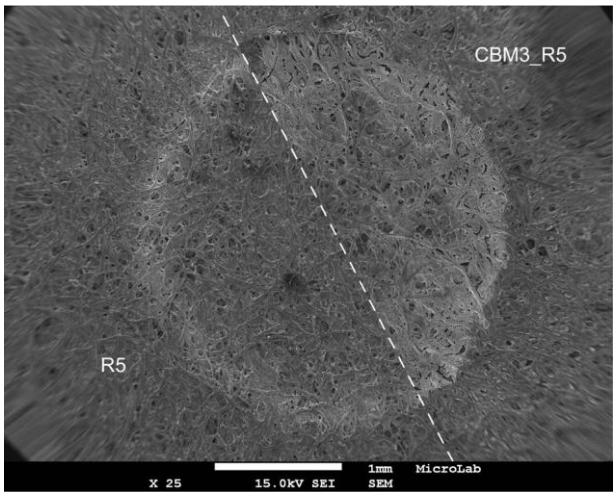

Figure 26. Composite image of SEM micrographs of circular areas of paper prepared with 3000 nmol of R5 (left) and CBM3-R5 (right), and after immersion on a 91 mM silicic acid solution for 5 min. The formation of silica over paper is apparent by the presence of a whitish material that contrasts strongly with the paper background. Scale bar of 1 mm.

SEM micrographs obtained at higher magnifications show that the morphology of the precipitated silica obtained with R5 and CBM3-R5 is very similar (Figure 27). The images show the presence of a densely packed network of fused and clustered silica particles laying over the network of cellulose fibers and fibrils characteristic of the paper matrix. The individual particles obtained with R5 (Figure 27A, C) had an average size of about 213±78 nm and individual particles obtained with CBM3-R5 (figure 27 B, C) had an average size of about 231±39 nm.

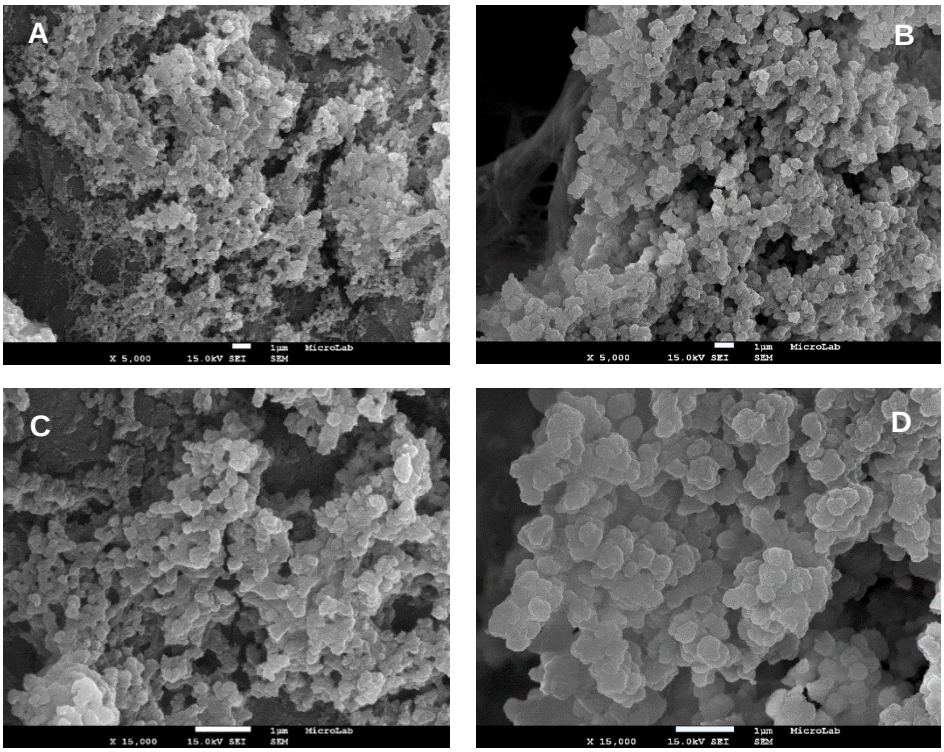

Figure 27. SEM micrographs of circular areas of paper prepared with 3000 pmol of R5 (left) and CBM3-R5 (right), and after immersion on a 91 mM silicic acid solution for 5 min. Micrographs were obtained with magnifications of x 5, 000 (A, B) and x 15, 000 (C, D). Scale bar of 1 µm.

Attempts were also made to precipitate silica over paper using lower amounts of R5 and CBM3-R5 (Table 6) in order to decrease particle density and eventually change morphology. However, precipitation was only observed with an amount of 3 pmol of R5 (Figure 28). As expected, the silica particles obtained in this case were more individualized and dispersed over the cellulose fibers and no formation of dense aggregates of silica were observed, as found with 3 000 pmol of R5 and CBM-R5 (Figure 27). The mean diameter of the spherical SiNPs was 228 ± 42 nm (Figure 28A). No precipitation of SiNPs over the cellulose fibers for 30 pmol either of R5 or CBM-R5. These results were not expected because the 3 pmol of R5 peptide was able to promote silica precipitation on the paper, in contrast with 30 pmol. Thus, it should be made more tests to overcome this problem.

Table 6. Summary of the results on the paper assay.

Time of the reaction (min)	Final concentration of silicic acid in 50 mM phosphate buffer pH 7	Volume of the reaction per sample (the 2 mL of micro centrifuge)	Concentrations of the protein	Results	
				R5	CBM3-R5
5	91 mM	1 mL	3 000 pmol	**Yes**	**Yes**
			30 pmol	**No**	**No**
			3 pmol	**No/Yes**	**No**

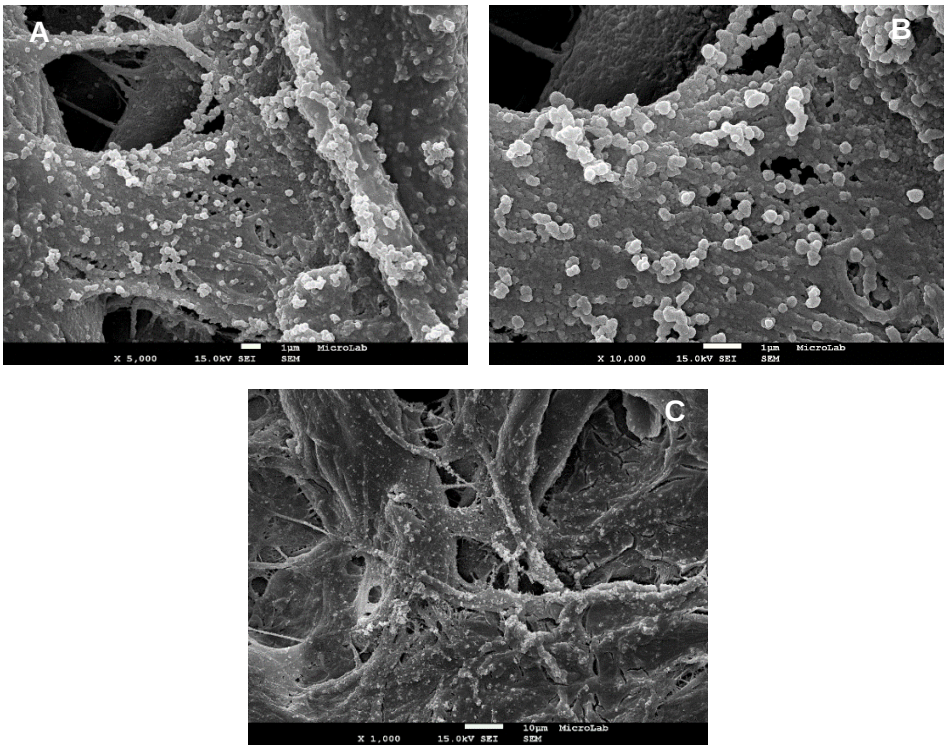

Figure 28. SEM micrographs of circular areas of paper prepared with 3 pmol of R5 after immersion on a 91 mM silicic acid solution for 5 min. A, B, C micrographs are presented with magnifications of x 5, 000, x 10, 000 and x 1, 000, respectively. Scale bar of 1 µm.

In contrast to what was observed for silica, the titanium dioxide nanoparticles were not detected over the cellulose fibers of paper by SEM analysis. This result was not expected because CBM3-R5

protein has shown titanium dioxide activity in the solution (Figure 24). Even though both conditions were the same for silica and titanium, the obtained results were not conclusive. Thus, more assays should be repeated in an attempt to overcome this problem.

5. Conclusions

Nanotechnology has been crucial for the development of new and innovative materials and devices with applications in different fields such as biomedical, agriculture, energy, electronic. The goal of this work was to produce silica and titanium dioxide nanoparticles under mild conditions through the use of a fusion of the silica precipitating peptide R5 with the carbohydrate binding module CBM3 in order to create cellulose-inorganic hybrid composite with new functions.

As a first step towards this goal, the R5-induced precipitation of silica and titanium dioxide nanoparticles in solution was studied. Under the conditions studied (1.5 mM R5, 91 mM precursor, 50 mM phosphate buffer pH 7, 5 minutes), 71% and 50% of the silica and titanium dioxide precursors precipitated. The specific activity of R5 for silica and titanium dioxide precipitation was 8.6 ± 2.2 nmol Si/min.nmol R5 and 6.0 ± 1.0 nmol Ti/ min.nmol R5, respectively. SEM analysis showed that precipitates were composed of close to spherical nanoparticles with individual sizes in the range of 37 to 538 nm for silica and for titanium dioxide was in the order of 479 nm. Extensive agglomerates of fused nanoparticles were observed in both cases. Next, a CBM3-R5 fusion was successfully designed, produced and purified. Experiments conducted in solution confirmed that R5 did not lose its ability to precipitate silica and titanium dioxide in solution after being fused to CBM3. The morphology and sizes of the obtained nanoparticles were equivalent to the ones obtained with R5 alone.

In the second part of this work, the ability of R5 and CBM-R5 to precipitate silica and titanium dioxide *in situ*, over cellulose fibers of chromatographic paper was investigated. When used at a density of 3000 pmol/0.13 cm^2, both pre-immobilized R5 (via physical adsorption) and CBM3-R5 (by affinity interactions) were able to precipitate silica, yielding densely packed networks of fused and clustered particles over the cellulose fibers and fibrils in paper. Individual particles obtained with R5 and CBM3-R5 had an average size of around 213±78 nm and 231±39 nm, respectively. Precipitation of silica was not observed when lowering the amount of protein to 30 pmol and 3 pmol per 0.13 cm^2, with the exception of 3 pmol of R5. In this case, silica nanoparticles (228 ± 42 nm) were more individualized and dispersed over the cellulose fibers and no formation of dense aggregates of silica were observed. These experiments should be repeated, since there is no apparent reason for not observing precipitation at 30 pmol per 0.13 cm^2. In the case of titanium dioxide, no precipitation was observed over the cellulose fibers.

In future experiments, intermediate protein concentrations (e.g. 300 pmol per 0.13 cm^2) should be tested in order to evaluate the influence of the protein amount for silica precipitation on the cellulose fibers. Also, the precipitation reaction could be promoted by pipetting 1 µl or more of the precursor solution instead of immersing the paper in precursor solution, in order to better control the process. This experiment was made in this work, but the results were not evaluated because the main focus of this thesis was to analyze the papers from the immersion method. Another analyze that could be made is to determine the specific precipitation activity of CBM3-R5 in solution for both inorganic materials (silica and titanium dioxide).

Also, other abilities of the R5 could be explored on the paper, for example used R5 as template in order to create gold nanostructures on the paper and evaluate their catalytic properties. In the advanced stage of this project, the properties of R5 and gold have already been explored, which revealed promising results.

About future applications with SCH, surface of silica could be functionalized with linker molecules for example amine, thiol among others in other to attachment of biomolecule to the silica surface (Ali et al., 2014). Thus can be used to create a based paper biosensor. The same could be made with titanium dioxide through the use of the silanes or carboxylic groups (Trino et al., 2016).

References

Abdul Rashid, S.; Othman, S. H.; Mohd Ghazi, T. I.; Abdullah, N. Effect of Postdeposition Heat Treatment on the Crystallinity, Size, and Photocatalytic Activity of TiO_2 Nanoparticles Produced via Chemical Vapour Deposition. *J. Nanomater.* **2010**, *2010*, 1–10.

Abdullahil, K.; Maniruzzaman, M.; Kan, B.-W.; Kim, J. Fabrication and Characterization of Titanium Dioxide-Cellulose Composite and Its Urea Biosensing Behavior. **2015**, *27* (7), 539–548.

Adachi, M.; Tsukui, S.; Okuyama, K. Nanoparticle Formation Mechanism in CVD Reactor with Ionization of Source Vapor. *J. Nanoparticle Res.* **2003**, *5* (1), 31–37.

Akarsu, M.; Asiltörk, M.; Sayilkan, F.; Kiraz, N.; Arpac, E.; Sayilkan, H. A Novel Approach to the Hydrothermal Synthesis of Anatase Titania Nanoparticles and the Photocatalytic Degradation of Rhodamine B. *Turkish J. Chem.* **2006**, *30* (3), 333–343.

Ali, Y.; Zohre, R.; Mostafa, J.; Samaneh, R. Dye-Doped Fluorescent Nanoparticles in Molecular Imaging : A Review of Recent Advances and Future Opportunities. **2014**, *11* (2), 102–113.

Arfi, Y.; Shamshoum, M.; Rogachev, I.; Peleg, Y.; Bayer, E. A. Integration of Bacterial Lytic Polysaccharide Monooxygenases into Designer Cellulosomes Promotes Enhanced Cellulose Degradation. *Proc. Natl. Acad. Sci.* **2014**, *111* (25), 9109–9114.

Auffan, M.; Rose, J.; Bottero, J.-Y.; Lowry, G. V; Jolivet, J.-P.; Wiesner, M. R. Towards a Definition of Inorganic Nanoparticles from an Environmental, Health and Safety Perspective. *Nat. Nanotechnol.* **2009**, *4* (10), 634–641.

AZoNano. Silicon Dioxide, Silica (SiO_2) Nanoparticles – Properties, Applications http://www.azonano.com/article.aspx?ArticleID=3398 (accessed Feb 28, 2016).

Babu, E.; Mareeswaran, P. M.; Rajagopal, S. Highly Sensitive Optical Biosensor for Thrombin Based on Structure Switching Aptamer-Luminescent Silica Nanoparticles. *J. Fluoresc.* **2013**, *23* (1), 137–146.

Barndõk, H.; Hermosilla, D.; Han, C.; Dionysiou, D. D.; Negro, C.; Blanco, Á. Degradation of 1,4-Dioxane from Industrial Wastewater by Solar Photocatalysis Using Immobilized NF-TiO2 Composite with Monodisperse TiO2 Nanoparticles. *Appl. Catal. B Environ.* **2016**, *180*, 44–52.

Bayer, E. a; Shimon, L. J. W.; Shoham, Y.; Lamed, R. Cellulosomes—Structure and Ultrastructure. *J. Struct. Biol.* **1998**, *124* (2-3), 221–234.

Bhandari, R.; Knecht, M. R. Synthesis, Characterization, and Catalytic Application of Networked Au Nanostructures Fabricated Using Peptide Templates. *Catal. Sci. Technol.* **2012**, *2* (7), 1360.

Blake, A. W.; McCartney, L.; Flint, J. E.; Bolam, D. N.; Boraston, A. B.; Gilbert, H. J.; Knox, J. P. Understanding the Biological Rationale for the Diversity of Cellulose-Directed Carbohydrate-Binding Modules in Prokaryotic Enzymes. *J. Biol. Chem.* **2006**, *281* (39), 29321–29329.

Bolam, D. N.; Ciruela, A.; McQueen-Mason, S.; Simpson, P.; Williamson, M. P.; Rixon, J. E.; Boraston, A.; Hazlewood, G. P.; Gilbert, H. J. Pseudomonas Cellulose-Binding Domains Mediate Their Effects by Increasing Enzyme Substrate Proximity. *Biochem. J.* **1998**, *331* (3), 775–781.

van Bommel, K. J. C.; Friggeri, A.; Shinkai, S. Organic Templates for the Generation of Inorganic Materials. *Angew. Chemie Int. Ed.* **2003**, *42* (9), 980–999.

Boraston, A. B.; Bolam, D. N.; Gilbert, H. J.; Davies, G. J. Carbohydrate-Binding Modules: Fine-Tuning Polysaccharide Recognition. *Biochem. J.* **2004**, *382* (3), 769–781.

Branda, F. The Sol-Gel Route to Nanocomposites. In *Advances in Nanocomposites - Synthesis, Characterization and Industrial Applications*; InTech, 2011; Vol. 14, pp 323–340.

Brott, L. L.; Naik, R. R.; Pikas, D. J.; Kirkpatrick, S. M.; Tomlin, D. W.; Whitlock, P. W.; Clarson, S. J.; Stone, M. O. Ultrafast Holographic Nanopatterning of Biocatalytically Formed Silica. *Nature* **2001**, *413* (6853), 291–293.

Brümmer, F. Living inside a Glass Box-Silica in Diatoms. *Prog. Mol. Subcell. Biol.* **2003**, *33*, 3–10.

Buettner, K. M.; Valentine, A. M. Bioinorganic Chemistry of Titanium. *Chem. Rev.* **2012**, *112* (3), 1863–1881.

Burger, J. M.; Robinson, J. B.; Pease, F. L. Sol-Gel-Derived Nanoscale Materials. In *Handbook of nanoparticles*; Aliofkhazraei, M., Ed.; Springer International Publishing: Cham, 2015; pp 691–714.

Buzea, C.; Pacheco, I. I.; Robbie, K. Nanomaterials and Nanoparticles: Sources and Toxicity. *Biointerphases* **2007**, *2* (4), 17–71.

Carrilho, E.; Martinez, A. W.; Whitesides, G. M. Understanding Wax Printing: A Simple Micropatterning Process for Paper-Based Microfluidics. *Anal. Chem.* **2009**, *81* (16), 7091–7095.

Castelvetro, V.; De Vita, C. Nanostructured Hybrid Materials from Aqueous Polymer Dispersions. *Adv. Colloid Interface Sci.* **2004**, *108-109*, 167–185.

Choi, O.; Kim, B.-C.; An, J.-H.; Kyongseon, M.; Kim, Y. H.; Um, Y.; Oh, M.-K.; Sang, B.-I. A Biosensor Based on the Self-Entrapment of Glucose Oxidase within Biomimetic Silica Nanoparticles Induced by a Fusion Enzyme. *Ezyme Microb. Technol.* **2011**, *49* (5), 441–445.

Cole, K. E.; Ortiz, A. N.; Schoonen, M. A.; Valentine, A. M. Peptide- and Long-Chain Polyamine- Induced Synthesis of Micro- and Nanostructured Titanium Phosphate and Protein Encapsulation. *Chem. Mater.* **2006**, *18* (19), 4592–4599.

Coradin, T.; Eglin, D.; Livage, J. The Silicomolybdic Acid Spectrophotometric Method and Its Application to Silicate/biopolymer Interaction Studies. *Spectroscopy* **2004**, *18* (4), 567–576.

Daoud, W. A.; Xin, J. H.; Zhang, Y.-H. Surface Functionalization of Cellulose Fibers with Titanium Dioxide Nanoparticles and Their Combined Bactericidal Activities. *Surf. Sci.* **2005**, *599* (1-3), 69–75.

Degani, O.; Gepstein, S.; Dosoretz, C. G. A New Method for Measuring Scouring Efficiency of Natural Fibers Based on the Cellulose-Binding Domain-β-Glucuronidase Fused Protein. *J. Biotechnol.* **2004**, *107* (3), 265–273.

Demilecamps, A.; Reichenauer, G.; Rigacci, A.; Budtova, T. Cellulose–silica Composite Aerogels from "one-Pot" Synthesis. *Cellulose* **2014**, *21* (4), 2625–2636.

Ding, Y.; Chu, X.; Hong, X.; Zou, P.; Liu, Y. The Infrared Fingerprint Signals of Silica Nanoparticles and Its Application in Immunoassay. *Appl. Phys. Lett.* **2012**, *100* (1), 1–3.

Dolatabadi, J. E. N.; de la Guardia, M. Applications of Diatoms and Silica Nanotechnology in Biosensing, Drug and Gene Delivery, and Formation of Complex Metal Nanostructures. *TrAC Trends Anal. Chem.* **2011**, *30* (9), 1538–1548.

Ducheyne, P.; Ducheyne, P.; Kevin, H.; Hutmacher, E. D.; Grainger, W. D.; Kirkpatrick, J. C. *Comprehensive Biomaterials*, 1st ed.; Elsevier Science Ltd, 2011;pp 1-3672.

Edwards, J. S.; Kumbhar, A.; Roberts, A.; Hemmert, A. C.; Carol, C.; Potter, P. M.; Redinbo, M. R. Immobilization of Active Human Carboxylesterase 1 in Biomimetic Silica Nanoparticles. **2013**, *27* (3), 863–869.

Emond, S.; Guieysse, D.; Lechevallier, S.; Dexpert-Ghys, J.; Monsan, P.; Remaud-Siméon, M. Alteration of Enzyme Activity and Enantioselectivity by Biomimetic Encapsulation in Silica Particles. *Chem. Commun.* **2012**, *48* (9), 1314–1316.

Filipponi, L.; Sutherlan, D. Nanotechnology: A Brief Introduction. *Nanocap* **2007**, 1–11.

Finnie, K. S.; Bartlett, J. R.; Barb, C. J. A.; Kong, L.; Barbe, C. J. A. Formation of Silica Nanoparticles in Microemulsions Formation of Silica Nanoparticles in Microemulsions. **2007**, *23* (6), 3017–3024.

Georgelis, N.; Yennawar, N. H.; Cosgrove, D. J. Structural Basis for Entropy-Driven Cellulose Binding by a Type-A Cellulose-Binding Module (CBM) and Bacterial Expansin. *Proc. Natl. Acad. Sci.* **2012**, *109* (37), 14830–14835.

Gholami, T.; Salavati-Niasari, M.; Bazarganipour, M.; Noori, E. Synthesis and Characterization of Spherical Silica Nanoparticles by Modified Stöber Process Assisted by Organic Ligand. *Superlattices Microstruct.* **2013**, *61*, 33–41.

Ghosh, D.; Mondal, S.; Ghosh, S.; Saha, A. Protein Conformation Driven Biomimetic Synthesis of Semiconductor Nanoparticles. *J. Mater. Chem.* **2012**, *22* (2), 699–706.

Gordon, R.; Losic, D.; Tiffany, M. A.; Nagy, S. S.; Sterrenburg, F. A. S. The Glass Menagerie: Diatoms for Novel Applications in Nanotechnology. *Trends Biotechnol.* **2009**, *27* (2), 116–127.

Grillo, R.; Rosa, A. H.; Fraceto, L. F. Engineered Nanoparticles and Organic Matter: A Review of the State-of-the-Art. *Chemosphere* **2015**, *119*, 608–619.

Gu, L.; Zhang, A.; Hou, K.; Dai, C.; Zhang, S.; Liu, M.; Song, C.; Guo, X. One-Pot Hydrothermal Synthesis of Mesoporous Silica Nanoparticles Using Formaldehyde as Growth Suppressant. *Microporous Mesoporous Mater.* **2012**, *152*, 9–15.

Guizard, C.; Bac, A.; Barboiu, M.; Hovnanian, N. Hybrid Organic-Inorganic Membranes with Specific Transport Properties: Application in Separation and Sensors Technologies. *Sep. Purif. Technol.* **2001**, *25* (1-3), 167–180.

Hashimoto, H. Recent Structural Studies of Carbohydrate-Binding Modules. *Cell. Mol. Life Sci.* **2006**, *63* (24), 2954–2967.

Hospes, M.; Hendriks, J.; Hellingwerf, K. J. Tryptophan Fluorescence as a Reporter for Structural Changes in Photoactive Yellow Protein Elicited by Photo-Activation. *Photochem. Photobiol. Sci.* **2013**, *12* (3), 479–488.

Jakhmola, A.; Bhandari, R.; Pacardo, D. B.; Knecht, M. R. Peptide Template Effects for the Synthesis and Catalytic Application of Pdnanoparticle Networks. *J. Mater. Chem.* **2010**, *20* (8), 1522–1531.

Jantschke, A.; Spinde, K.; Brunner, E. Electrostatic Interplay: The Interaction Triangle of Polyamines, Silicic Acid, and Phosphate Studied through Turbidity Measurements, Silicomolybdic Acid Test, and (29)Si NMR Spectroscopy. *Beilstein J. Nanotechnol.* **2014**, *5*, 2026–2035.

Jia, N.; Li, S. M.; Ma, M. G.; Zhu, J. F.; Sun, R. C. Synthesis and Characterization of Cellulose-Silica Composite Fiber in Ethanol/water Mixed Solvents. *BioResources* **2011**, *6* (2), 1186–1195.

Keshk, S. M. A. S.; Hamdy, M. S.; Badr, I. H. A. Physicochemical Characterization of Mercerized Cellulose / TiO 2 Nano-Composite. **2015**, *5* (1), 24–29.

Kimx, B.; Kang, S.-Y.; Kim, D.; Moon, S.; Park, E.; Kang, K. Analysis of Photoluminescent Chromophores Obtained from a Cellulose Acetate and Silica Sphere Composite. *J. Non. Cryst. Solids* **2015**, *412*, 45–48.

Knecht, M. R.; Wright, D. W. Functional Analysis of the Biomimetic Silica Precipitating Activity of the R5 Peptide from *Cylindrotheca Fusiformis*. *Chemical Communications*. 2003, pp 3038–3039.

Kröger, N. Prescribing Diatom Morphology: Toward Genetic Engineering of Biological Nanomaterials. *Curr. Opin. Chem. Biol.* **2007**, *11* (6), 662–669.

Kröger, N.; Brunner, E. Complex-Shaped Microbial Biominerals for Nanotechnology. *Wiley Interdiscip. Rev. Nanomedicine Nanobiotechnology* **2014**, *6* (6), 615–627.

Kröger, N.; Deutzmann, R.; Sumper, M. Polycationic Peptides from Diatom Biosilica That Direct Silica Nanosphere Formation. *Science (80-.).* **1999**, *286* (5442), 1129–1132.

Kröger, N.; Deutzmann, R.; Bergsdorf, C.; Sumper, M. Species-Specific Polyamines from Diatoms Control Silica Morphology. *Proc. Natl. Acad. Sci.* **2000**, *97* (26), 14133–14138.

Kröger, N.; Deutzmann, R.; Sumper, M. Silica-Precipitating Peptides from Diatoms: The Chemical Structure of Silaffin-1A from Cylindrotheca Fusiformis. *J. Biol. Chem.* **2001**, *276* (28), 26066–26070.

Kröger, N.; Lorenz, S.; Brunner, E.; Sumper, M. Self-Assembly of Highly Phosphorylated Silaffins and Their Function in Biosilica Morphogenesis. *Science.*. **2002**, *298* (5593), 584–586.

Lechner, C. C.; Becker, C. F. W. A Sequence-Function Analysis of the Silica Precipitating Silaffin R5 Peptide. *J. Pept. Sci.* **2014**, *20* (2), 152–158.

Lechner, C. Functional Analysis and Biotechnological Applications of Silaffin Peptides, Technische Universität München, 2013.

Lechner, C.; Becker, C. Silaffins in Silica Biomineralization and Biomimetic Silica Precipitation. *Mar. Drugs* **2015**, *13* (8), 5297–5333.

Lehtiö, J.; Sugiyama, J.; Gustavsson, M.; Fransson, L.; Linder, M.; Teeri, T. T. The Binding Specificity and Affinity Determinants of Family 1 and Family 3 Cellulose Binding Modules. *Proc. Natl. Acad. Sci.* **2003**, *100* (2), 484–489.

Li, M.; Yin, J.-J.; Wamer, W. G.; Lo, Y. M. Mechanistic Characterization of Titanium Dioxide Nanoparticle-Induced Toxicity Using Electron Spin Resonance. *J. Food Drug Anal.* **2014a**, *22* (1), 76–85.

Li, Y.; Wang, H.; Liu, X.; Guo, L.; Ji, X.; Wang, L.; Tian, D.; Yang, X. Nonenzymatic Nitrite Sensor Based on a Titanium Dioxide Nanoparticles/ionic Liquid Composite Electrode. *J. Electroanal. Chem.* **2014b**, *719*, 35–40.

Li, Z.; Percival, S. S.; Bonard, S.; Gu, L. Fabrication of Nanoparticles Using Partially Purified Pomegranate Ellagitannins and Gelatin and Their Apoptotic Effects. *Mol. Nutr. Food Res.* **2011**, *55* (7), 1096–1103.

Ling, H.; Kim, K.; Liu, Z.; Shi, J.; Zhu, X.; Huang, J. Photocatalytic Degradation of Phenol in Water on as-Prepared and Surface Modified TiO2 Nanoparticles. *Catal. Today* **2015**, *258*, 96–102.

Liu, Y.-C.; Lu, Y.-F.; Zeng, Y.-Z.; Liao, C.-H.; Chung, J.-C.; Wei, T.-Y. Nanostructured Mesoporous Titanium Dioxide Thin Film Prepared by Sol-Gel Method for Dye-Sensitized Solar Cell. *Int. J. Photoenergy* **2011**, *2011*, 1–9.

Lohman, K. The Ubiquitous Diatom–A Brief Survey Of The Present State Of Knowledge. *Am. J. Sci. A*. 1960, pp 180–191.

Lovingood, D. D.; Owens, J. R.; Seeber, M.; Kornev, K. G.; Luzinov, I. Preparation of Silica Nanoparticles Through Microwave-Assisted Acid-Catalysis. *J. Vis. Exp.* **2013**, No. 82, 1–9.

Malvern instruments. *Zetasizer Nano Series User Manual*; 2004.

Mangematin, V.; Walsh, S. The Future of Nanotechnologies. *Technovation* **2012**, *32* (3-4), 157–160.

Maniruzzaman, M.; Jang, S. D.; Kim, J. Titanium Dioxide-Cellulose Hybrid Nanocomposite and Its Glucose Biosensor Application. *Mater. Sci. Eng. B Solid-State Mater. Adv. Technol.* **2012**, *177* (11), 844–848.

Messori, M.; Toselli, M.; Pilati, F.; Mascia, L.; Tonelli, C. Synthesis and Characterisation of Silica Hybrids Based on Poly(ε-Caprolactone-B-Perfluoropolyether-B-ε-Caprolactone). *Eur. Polym. J.* **2002**, *38* (6), 1129–1136.

Moharir, A.V., Sarma, K.A., Murti Krishna, R. S. R. Spectrophotometric Determination of Titanium with Tiron. **1972**, *17*, 167–172.

Naghsh, M.; Sadeghi, M.; Moheb, A.; Chenar, M. P.; Mohagheghian, M. Separation of Ethylene/ethane and Propylene/propane by Cellulose Acetate–silica Nanocomposite Membranes. *J. Memb. Sci.* **2012**, *423-424*, 97–106.

Naik, R. R.; Whitlock, P. W.; Rodriguez, F.; Brott, L. L.; Glawe, D. D.; Clarson, S. J.; Stone, M. O. Controlled Formation of Biosilica Structures *in Vitro*. *Chem. Commun.* **2003**, No. 2, 238–239.

Nam, D. H.; Won, K.; Kim, Y. H.; Sang, B. I. A Novel Route for Immobilization of Proteins to Silica Particles Incorporating Silaffin Domains. *Biotechnol. Prog.* **2009**, *25* (6), 1643–1649.

Nelson, L. D.; Cox, M. M. *Lehninger Principles of Biochemistry*, 4th ed.; W. H. Freeman: New York, 2004.

Nelson, M. D.; Arrington, M. J. SOP for Analyzing Silicate (Microscale) by Using Manual Colorimetric Method. **2010**, 4–6.

Niemelä, E.; Desai, D.; Nkizinkiko, Y.; Eriksson, J. E.; Rosenholm, J. M. Sugar-Decorated Mesoporous Silica Nanoparticles as Delivery Vehicles for the Poorly Soluble Drug Celastrol Enables Targeted Induction of Apoptosis in Cancer Cells. *Eur. J. Pharm. Biopharm.* **2015**, *96*, 11–21.

Nobbmann, U.; Morfesis, A. Light Scattering and Nanoparticles. *Mater. Today* **2009**, *12* (5), 52–54.

Nowack, B.; Bucheli, T. D. Occurrence, Behavior and Effects of Nanoparticles in the Environment. *Environ. Pollut.* **2007**, *150* (1), 5–22.

Oliveira, C.; Carvalho, V.; Domingues, L.; Gama, F. M. Recombinant CBM-Fusion Technology — Applications Overview. *Biotechnol. Adv.* **2015**, *33* (3-4), 358–369.

Otzen, D. The Role of Proteins in Biosilicification. *Scientifica (Cairo).* **2012**, *2012*, 1–22.

Owens, G. J.; Singh, R. K.; Foroutan, F.; Alqaysi, M.; Han, C.-M.; Mahapatra, C.; Kim, H.-W.; Knowles, J. C. Sol–gel Based Materials for Biomedical Applications. *Prog. Mater. Sci.* **2016**, *77*, 1–79.

Parkinson, J.; Gordon, R. Beyond Micromachining: The Potential of Diatoms. *Trends Biotechnol.* **1999**, *17* (5), 190–196.

Patwardhan, S. V; Clarson, S. J. Silicification and Biosilicification Part 3. The Role of Synthetic Polymers and Polypeptides at Neutral pH. *Silicon Chem.* **2002a**, *1* (3), 207–214.

Patwardhan, S. V; Clarson, S. J. Silicification and Biosilicification Part 7: Poly-L-Arginine Mediated Bioinspired Synthesis of Silica. *J. Inorg. Organomet. Polym.* **2003**, *13* (4), 193–203.

Patwardhan, S. V; Mukherjee, N.; Clarson, S. J. The Use of Poly-L-Lysine to Form Novel Silica Morphologies and the Role of Polypeptides in Biosilicification. *J. Inorg. Organomet. Polym.* **2001**, *11* (3), 193–198.

Patwardhan, S. V; Mukherjee, N.; Steintz-Kannan, M.; Clarson, S. J. Bioinspired Synthesis of New Silica Structures. *Chem. Commun. (Camb).* **2003**, No. 10, 1122–1123.

Patwardhan, S. V; Shiba, K.; Schroder, H. C.; Muller, W. E. G.; Clarson, S. J.; Perry, C. C. The Interaction of "Silicon" with Proteins: Part 2. The Rold of Bioinspired Peptide and Recombinant Proteins in Silica Polymerization. *Sci. Technol. Silicones Silicone-Modified Mater.* **2007**, *964*, 328–347.

Patwardhan, S. V.; Clarson, S. J. Effect of Template Size on the Formation of Silica. *J. Inorg. Organomet. Polym.* **2002b**, *12* (3), 109–116.

Patwardhan, S. V.; Clarson, S. J.; Perry, C. P. On the Role(s) of Additives in Bioinspired Silicification. *Chem. Commun.* **2005**, *9*, 1113–1121.

Pender, M. J.; Sowards, L. A.; Hartgerink, J. D.; Stone, M. O.; Naik, R. R. Peptide-Mediated Formation of Single-Wall Carbon Nanotube Composites. *Nano Lett.* **2006**, *6* (1), 40–44.

Pértile, R.; Moreira, S.; Andrade, F.; Domingues, L.; Gama, M. Bacterial Cellulose Modified Using Recombinant Proteins to Improve Neuronal and Mesenchymal Cell Adhesion. *Biotechnol. Prog.* **2012**, *28* (2), 526–532.

Pierre, A. C. Introduction to Sol-Gel Processing. In *The Kluwer International Series in Sol-Gel Processing: Technology and Applications*; Klein, L., Ed.; Springer Science+ Business Media, LLC: New York, 1998;pp 1-386.

Ping, L.; Xian, C.; Mao, Z.; Zhu, Q. Synthesis and Characteri Zation of Titania Nanoparticles by Microemulsion Process. **2006**, *45* (September), 17–20.

Poulsen, N.; Sumper, M.; Kröger, N. Biosilica Formation in Diatoms: Characterization of Native Silaffin-2 and Its Role in Silica Morphogenesis. *Proc. Natl. Acad. Sci.* **2003**, *100* (21), 12075–12080.

Prathna, T. C.; Mathew, L.; Chandrasekaran, N.; Raichur, M. A.; Mukherjee, A. Biomimetic Synthesis of Nanoparticles: Science, Technology & Applicability. In *Biomimetics Learning from Nature*; Mukherjee, A., Ed.; InTech, 2010; pp 1–20.

Qhobosheane, M.; Santra, S.; Zhang, P.; Tan, W. Biochemically Functionalized Silica Nanoparticles. *Analyst* **2001**, *126* (8), 1274–1278.

Rahman, I. A.; Padavettan, V. Synthesis of Silica Nanoparticles by Sol-Gel: Size-Dependent Properties, Surface Modification, and Applications in Silica-Polymer Nanocomposites—A Review. *J. Nanomater.* **2012**, *2012*, 1–15.

Rahman, I. A.; Vejayakumaran, P.; Sipaut, C. S.; Ismail, J.; Chee, C. K. Size-Dependent Physicochemical and Optical Properties of Silica Nanoparticles. *Mater. Chem. Phys.* **2009**, *114* (1), 328–332.

Raman, N.; Sudharsan, S.; Pothiraj, K. Synthesis and Structural Reactivity of Inorganic–organic Hybrid Nanocomposites – A Review. *J. Saudi Chem. Soc.* **2012**, *16* (4), 339–352.

Ramsden, J. J. What Is Nanotechnology? In *Nanotechnology - An introduction*; Elsevier Inc., 2011; pp 1–14.

Rezaei, S.; Manoucheri, I.; Moradian, R.; Pourabbas, B. One-Step Chemical Vapor Deposition and Modification of Silica Nanoparticles at the Lowest Possible Temperature and Superhydrophobic Surface Fabrication. *Chem. Eng. J.* **2014**, *252*, 11–16.

Rodríguez, F.; Glawe, D. D.; Naik, R. R.; Hallinan, K. P.; Stone, M. O. Study of the Chemical and Physical Influences upon in Vitro Peptide-Mediated Silica Formation. *Biomacromolecules* **2004**, *5* (2), 261–265.

Rosa, A.; Louro, F.; Martins, S.; Inácio, J.; Azevedo, A.; Prazeres, M. Capture and Detection of DNA Hybrids on Paper via the Anchoring of Antibodies with Fusions of Carbohydrate Binding Modules and ZZ-Domains. *Anal. Chem.* **2014**, *86* (9), 4340–4347.

Rossi, L. M.; Shi, L.; Quina, F. H.; Rosenzweig, Z. Stöber Synthesis of Monodispersed Luminescent Silica Nanoparticles for Bioanalytical Assays. *Langmuir* **2005**, *21* (10), 4277–4280.

Sanpo, N. *Solution Precursor Plasma Spray System*; Springer Briefs in Materials, 2014.

Sayes, M. C.; Wahi, R.; Kurian, A. P.; Liu, Y.; West, L. J.; Ausman, D. K.; Warheit, B. D.; Colving, L. V. Correlating Nanoscale Titania Structure with Toxicity: A Cytotoxicity and Inflammatory Response Study with Human Dermal Fibroblasts and Human Lung Epithelial Cells. *Toxicol. Sci.* **2006**, *92* (1), 174–185.

Schlipf, D. M.; Jones, C. A.; Armbruster, M. E.; Rushing, E. S.; Wooten, K. C.; Rankin, S. E.; Knutson, B. L. Flavonoid Adsorption and Stability on Titania-Functionalized Silica Nanoparticles. *Colloids Surfaces A Physicochem. Eng. Asp.* **2015**, *478*, 15–21.

Schwarz, W. H.; Zverlov, V. V.; Bahl, H. Extracellular Glycosyl Hydrolases from *Clostridia.* In *Advances in Applied Microbiology*; 2004; Vol. 56, pp 215–261.

Senior, L.; Crump, M. P.; Williams, C.; Booth, P. J.; Mann, S.; Perriman, A. W.; Curnow, P. Structure and Function of the Silicifying Peptide R5. *J. Mater. Chem. B* **2015**, *3* (13), 2607–2614.

Sequeira, S.; Evtuguin, D. V.; Portugal, I. Preparation and Properties of Cellulose/silica Hybrid Composites. *Polym. Compos.* **2009**, *30* (9), 1275–1282.

Sewell, S. L.; Wright, D. W. Biomimetic Synthesis of Titanium Dioxide Utilizing the R5 Peptide Derived from Cylindrotheca F Usiformis. *Chem. Mater.* **2006**, *18* (13), 3108–3113.

Seyghali, B.; Zanjanchi, M. A. Photocatalytic Activity of TiO_2 Nanoparticles Synthesized in Presence of Ammonium Hexafluorosilicate. *Spectrochim. Acta Part A Mol. Biomol. Spectrosc.* **2015**, *151*, 104–110.

Shi, H.; Magaye, R.; Castranova, V.; Zhao, J. Titanium Dioxide Nanoparticles: A Review of Current Toxicological Data. *Part. Fibre Toxicol.* **2013**, *10* (1), 1–33.

Shoseyov, O.; Shani, Z.; Levy, I. Carbohydrate Binding Modules: Biochemical Properties and Novel Applications. *Microbiol. Mol. Biol. Rev.* **2006**, *70* (2), 283–295.

Smijs, T.; Pavel, S. Titanium Dioxide and Zinc Oxide Nanoparticles in Sunscreens: Focus on Their Safety and Effectiveness. *Nanotechnol. Sci. Appl.* **2011**, *4* (1), 95–112.

Song, M.; Zhang, R.; Wang, X. Nano-Titanium Dioxide Enhanced Biosensing of the Interaction of Dacarbazine with DNA and DNA Bases. *Mater. Lett.* **2006**, *60* (17-18), 2143–2147.

Stöber, W.; Fink, A.; Bohn, E. Controlled Growth of Monodisperse Silica Spheres in the Micron Size Range. *J. Colloid Interface Sci.* **1968**, *26* (1), 62–69.

Sumper, M.; Kröger, N. Silica Formation in Diatoms: The Function of Long-Chain Polyamines and Silaffins. *J. Mater. Chem.* **2004**, *14* (14), 2059–2065.

Svensson, A.; Nicklasson, E.; Harrah, T.; Panilaitis, B.; Kaplan, D. L.; Brittberg, M.; Gatenholm, P. Bacterial Cellulose as a Potential Scaffold for Tissue Engineering of Cartilage. *Biomaterials* **2005**, *26* (4), 419–431.

Taha, A. A.; Wu, Y.; Wang, H.; Li, F. Preparation and Application of Functionalized Cellulose Acetate/silica Composite Nanofibrous Membrane via Electrospinning for Cr(VI) Ion Removal from Aqueous Solution. *J. Environ. Manage.* **2012**, *112*, 10–16.

Tamba, B. I.; Dondas, A.; Leon, M.; Neagu, A. N.; Dodi, G.; Stefanescu, C.; Tijani, A. Silica Nanoparticles: Preparation, Characterization and *in Vitro/in Vivo* Biodistribution Studies. *Eur. J. Pharm. Sci.* **2015**, *71*, 46–55.

Thangavelu, K.; Annamalai, R.; Arulnandhi, D. Preparation and Characterization of Nanosized Tio 2 Powder by Sol-Gel Precipitation Route. *Int. J. Emerg. Technol. Adv. Eng.* **2013**, *3* (1), 636–639.

Thermo Fischer scientific Inc. INSTRUCTIONS BCA ™ Protein Assay Kit. *Publication Manual*. 2002, pp 1–7.

Thermo Fischer scientific Inc. Instructions Pierce Concentrator, PES, 3K, 10K, 30K and 100K MWCO; 0.5mL. 2014, pp 1–4.

Tomme, P.; Creagh, A. L.; Kilburn, D. G.; Haynes, C. A. Interaction of Polysaccharides with the N-Terminal Cellulose-Binding Domain of Cellulomonas Fimi CenC. 1. Binding Specificity and Calorimetric Analysis †. *Biochemistry* **1996**, *35* (44), 13885–13894.

Tormo, J.; Lamed, R.; Chirino, a J.; Morag, E.; Bayer, E. a; Shoham, Y.; Steitz, T. a. Crystal Structure of a Bacterial Family-III Cellulose-Binding Domain: A General Mechanism for Attachment to Cellulose. *EMBO J.* **1996**, *15* (21), 5739–5751.

Trino, D. L.; Ramachandran, A.; Lisboa-Filho, N. P.; Mathew, T. M.; George, A. Titanium Surface Biofunctionalization Using dmp1 Peptide Sequence: From Chemical Attachment to Osteogenic Differentiation Study; Montréa, 2016.

Uddin, M. J.; Cesano, F.; Bonino, F.; Bordiga, S.; Spoto, G.; Scarano, D.; Zecchina, A. Photoactive TiO_2 Films on Cellulose Fibres: Synthesis and Characterization. *J. Photochem. Photobiol. A Chem.* **2007**, *189* (2), 286–294.

Wang, K.; Liu, P.; Ye, Y.; Li, J.; Zhao, W.; Huang, X. Fabrication of a Novel Laccase Biosensor Based on Silica Nanoparticles Modified with Phytic Acid for Sensitive Detection of Dopamine. *Sensors Actuators B Chem.* **2014**, *197*, 292–299.

Xie, K.; Yu, Y.; Shi, Y. Synthesis and Characterization of Cellulose/silica Hybrid Materials with Chemical Crosslinking. *Carbohydr. Polym.* **2009**, *78* (4), 799–805.

Xu, T.; Song, C.; Liu, Y.; Han, G. Band Structures of TiO_2 Doped with N, C and B. *J. Zhejiang Univ. Sci. B* **2006**, *7* (4), 299–303.

Yaniv, O.; Morag, E.; Borovok, I.; Bayer, E. A.; Lamed, R.; Frolow, F.; Shimon, L. J. W. Structure of a Family 3a Carbohydrate-Binding Module from the Cellulosomal Scaffoldin CipA of *Clostridium Thermocellum* with Flanking Linkers: Implications for Cellulosome Structure. *Acta Crystallogr. Sect. F Struct. Biol. Cryst. Commun.* **2013**, *69* (7), 733–737.

Yaniv, O.; Fichman, G.; Borovok, I.; Shoham, Y.; Bayer, E. A.; Lamed, R.; Shimon, L. J. W.; Frolow, F. Fine-Structural Variance of Family 3 Carbohydrate-Binding Modules as Extracellular Biomass-Sensing Components of *Clostridium* Thermocellum Anti-σ I Factors. *Acta Crystallogr. Sect. D Biol. Crystallogr.* **2014**, *70* (2), 522–534.

Yazdimamaghani, M.; Pourvala, T.; Motamedi, E.; Fathi, B.; Vashaee, D.; Tayebi, L. Synthesis and Characterization of Encapsulated Nanosilica Particles with an Acrylic Copolymer by in Situ Emulsion Polymerization Using Thermoresponsive Nonionic Surfactant. *Materials (Basel).* **2013**, *6* (9), 3727–3741.

Yu, Q.; Wu, P.; Xu, P.; Li, L.; Liu, T.; Zhao, L. Synthesis of Cellulose/titanium Dioxide Hybrids in Supercritical Carbon Dioxide. *Green Chem.* **2008**, *10* (10), 1061–1067.

Zainizan Sahdan, M.; Nayan, N.; Haimi Dahlan, S.; Mahmoud, M. E.; Hashim, U. Sol-Gel Synthesis of TiO_2 Thin Films from In-House Nano-TiO_2 Powder. *Adv. Mater. Phys. Chem.* **2012**, *02* (04), 16–20.

Zallen, R.; Moret, M. P. The Optical Absorption Edge of Brookite TiO_2. *Solid State Commun.* **2006**, *137* (3), 154–157.

Zhang, R.; Zhang, Y.; Zhang, Q.; Xie, H.; Wang, H.; Nie, J.; Wen, Q.; Wei, F. Optical Visualization of Individual Ultralong Carbon Nanotubes by Chemical Vapour Deposition of Titanium Dioxide Nanoparticles. *Nat. Commun.* **2013**, *4*, 1727.

Appendix

1. Chromatographic purification of CBM3-R5

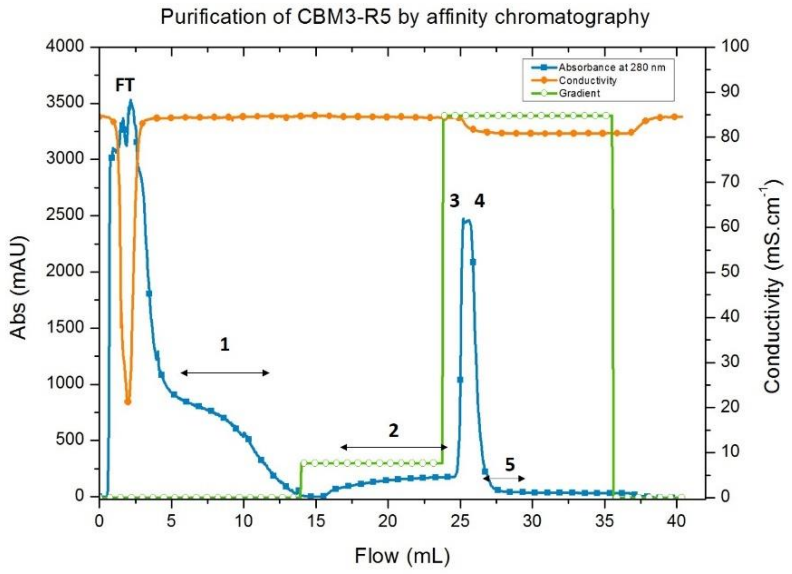

Figure 29 Purification of CBM3-R5 by niquel-affinity chromatography using a HisTrap FF column of 1mL in a Äkta 10 Purifier system (GE Healthcare). The column was equilibrated with 5 column volumes of buffer (10 mM imidazole, 50 mM NaHEPES, 1 M NaCl, 5 mM $CaCl_2$) and loaded with 1.8 mL of filtered supernatant. The column was washed with 20 column volume of the equilibration buffer and after with 20 column volumes of a similar buffer containing 35 mM imidazole. The bound CBM3-R5 protein was eluted with 20 column volumes of a buffer containing 300 mM imidazole and stored at -20ºC.

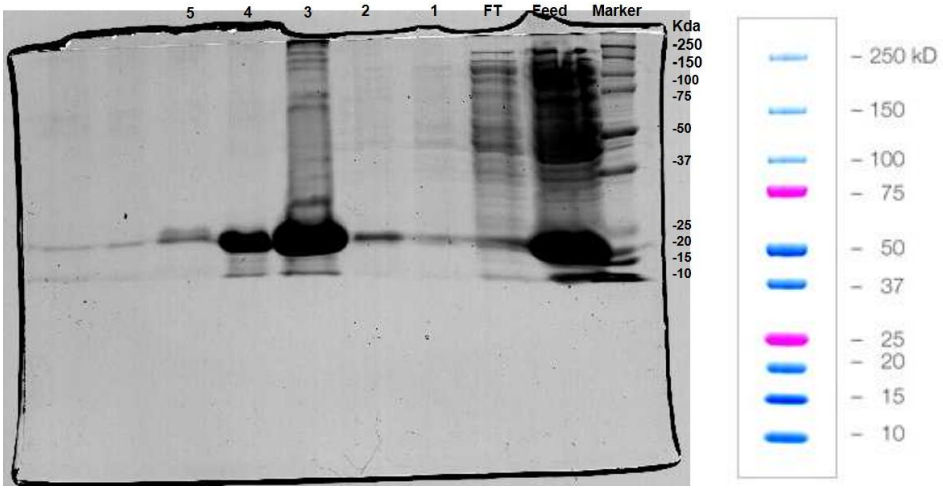

Figure 30 SDS-PAGE analysis of fractions collected during the chromatographic run shown in figure 29. The purified CBM3-R5 is found mainly in fractions 3 and 4. Image of the gel was obtained with a GS-800™ Calibrated Densitometer (Bio-Rad). The marker used was from Bio-Rad (250 Kda to 10 Kda. Molecular weight of CBM3-R5 is ~21 Kda.